#### **OPEN ACCESS**



# CO Excitation in High-z Main-sequence Analogues: Resolved CO(4-3)/CO(3-2) Line Ratios in DYNAMO Galaxies

Laura Lenkić 1,2 , Alberto D. Bolatto 1 , Deanne B. Fisher 3,4 , Roberto Abraham 5 , Karl Glazebrook 3,4 , Rodrigo Herrera-Camus 6 , Rebecca C. Levy 7,9 , Danail Obreschkow 8 , and Carolyn G. Volpert 1 Department of Astronomy, University of Maryland, College Park, MD 20742, USA; laura.lenkic@gmail.com 2 SOFIA Science Center, USRA, NASA Ames Research Center, M.S. N232-12, Moffett Field, CA 94035, USA 3 Centre for Astrophysics and Supercomputing, Swinburne University of Technology, PO Box 218, Hawthorn, VIC 3122, Australia 4 ARC Centre of Excellence for All Sky Astrophysics in 3 Dimensions (ASTRO 3D), Australia 5 Department of Astronomy & Astrophysics, University of Toronto, 50 St. George Street, Toronto, ON M5S 3H4, Canada 6 Departamento de Astronomía, Universidad de Concepción, Barrio Universitario, Concepción, Chile 7 Steward Observatory, University of Arizona, Tucson, AZ 85721, USA 8 International Centre for Radio Astronomy Research (ICRAR), University of Western Australia, Crawley, WA 6009, Australia Received 2022 August 8; revised 2023 January 8; accepted 2023 January 10; published 2023 March 1

# Abstract

The spectral line energy distribution of carbon monoxide contains information about the physical conditions of the star-forming molecular hydrogen gas; however, the relation to local radiation field properties is poorly constrained. Using  $\sim 1-2$  kpc scale Atacama Large Millimeter Array observations of CO(3-2) and CO(4-3), we characterize the CO(4-3)/CO(3-2) line ratios of local analogues of main-sequence galaxies at  $z \sim 1-2$ , drawn from the DYnamics of Newly Assembled Massive Objects (DYNAMO) sample. We measure CO(4-3)/CO(3-2) across the disk of each galaxy and find a median line ratio of  $R_{43} = 0.54^{+0.16}_{-0.15}$  for the sample. This is higher than literature estimates of local star-forming galaxies and is consistent with multiple lines of evidence that indicate DYNAMO galaxies, despite residing in the local universe, resemble main-sequence galaxies at  $z \sim 1-2$ . Comparing with existing lower-resolution CO(1-0) observations, we find  $R_{41}$  and  $R_{31}$  values in the range  $\sim$ 0.2-0.3 and  $\sim$ 0.4-0.8, respectively. We combine our kiloparsec-scale resolved line ratio measurements with Hubble Space Telescope observations of  $H\alpha$  to investigate the relation to the star formation rate surface density and compare this relation to expectations from models. We find increasing CO(4-3)/CO(3-2) with increasing star formation rate surface density; however, models overpredict the line ratios across the range of star formation rate surface densities we probe, in particular at the lower range. Finally, Stratospheric Observatory for Infrared Astronomy observations with the High-resolution Airborne Wideband Camera Plus and Field-Imaging Far-Infrared Line Spectrometer reveal low dust temperatures and no deficit of [CII] emission with respect to the total infrared luminosity.

Unified Astronomy Thesaurus concepts: Interstellar emissions (840); Extragalactic astronomy (506); Disk galaxies (391)

Supporting material: figure set

#### 1. Introduction

Molecular hydrogen gas (H<sub>2</sub>) is routinely mapped in high-redshift (high-z) galaxies with instruments such as the Atacama Large Millimeter/submillimeter Array (ALMA) and NOrthern Extended Millimeter Array (NOEMA) through the use of high rotational lines (high-J) of carbon monoxide (CO; see, e.g., Genzel et al. 2010; Tacconi et al. 2010; Decarli et al. 2014; Walter et al. 2016; Freundlich et al. 2019). High-J lines of CO can be used to address important topics such as the evolution of molecular gas reservoirs in galaxies across cosmic time (see, e.g., Walter et al. 2014; Decarli et al. 2016, 2019; Riechers et al. 2019; Lenkić et al. 2020). Mapping H<sub>2</sub> through high-J CO emission in high-z galaxies provides certain advantages over CO(1–0), because these lines are bright and allow for higher-resolution observations. However, the limited constraints of the CO excitation ladder, or the CO spectral line

Original content from this work may be used under the terms of the Creative Commons Attribution 4.0 licence. Any further distribution of this work must maintain attribution to the author(s) and the title of the work, journal citation and DOI.

energy distribution (SLED), render the conversion to the ground state transition, CO(1-0), uncertain. The CO excitation ladder contains information about the temperature and density of the  $H_2$  material (see, e.g., Carilli & Walter 2013, for a review), and understanding how those properties relate to local star formation activity will improve our understanding of how high-J CO lines map to CO(1-0) and  $H_2$  mass.

Several studies have characterized the CO excitation ladder in various local galaxy populations. In the Milky Way galactic center, observations from the Cosmic Background Explorer Far Infrared Absolute Spectrophotometer, which constrain the CO SLED from J=1-0 to J=8-7, show that the line ratios can be modeled with an excitation temperature of 40 K and that the CO SLED peaks at J=3 (Fixsen et al. 1999). A recent systematic study of CO(1-0) to CO(3-2) in nearby galaxies finds that the Rayleigh–Jeans brightness temperature ratios are generally higher in galaxy centers, decreasing with the radius and star formation rate (SFR) surface density (Leroy et al. 2022).

Kamenetzky et al. (2016) studied CO emission up to J=13-12 in ultraluminous infrared galaxies (ULIRGS; see also Greve et al. 2014), active galactic nuclei (AGN), and non-ULIRGs to find that CO SLEDs peak at increasingly high J

<sup>&</sup>lt;sup>9</sup> NSF Astronomy and Astrophysics Postdoctoral Fellow.

values with increasing far-infrared (FIR) luminosity, indicating that higher kinetic temperatures or densities are required (see also Figure 1 of Obreschkow et al. (2009), for how CO excitation depends on the galaxy type and excitation temperature). Observations of submillimeter galaxies (SMGs) show that they also have CO SLEDs with an "excess" of CO excitation with respect to the Milky Way; these generally rise up to  $J\!=\!5$  and then turn over for higher rotational states (Bothwell et al. 2013; Spilker et al. 2014). These high-excitation CO SLEDs suggest that alternative heating sources are required in these extreme galaxies such as mechanical heating via shocks, turbulence, or cosmic rays.

Although several large studies probe the CO SLEDs of extreme systems like SMGs and (Ultra) Luminous Infrared Galaxies (U/LIRGs), the CO SLEDs of normal  $z \sim 1-2$  starforming galaxies are not as well characterized. Valentino et al. (2020) conducted a large survey of mid- and high-J CO lines with ALMA in main-sequence galaxies at  $z \sim 1.1-1.7$ , and found that they have higher excitation than the Milky Way but are not quite as highly excited as ULIRGs, SMGs, or QSOs. Daddi et al. (2015) found similar results in a sample of four main-sequence near-IR-selected galaxies at  $z \sim 1.5$ , using CO(2-1), CO(3-2), and CO(5-4) observations. Bolatto et al. (2015) also presented the Rayleigh-Jeans brightness temperature CO(3-2)/CO(1-0) line ratio of four mainsequence galaxies observed with the Plateau de Bure Interferometer (PdBI), and found a ratio of about unity denoting high excitation. Finally, multiple case studies of the CO ladder in specific galaxies exist (see, e.g., Barvainis et al. 1997; van der Werf et al. 2010; Kamenetzky et al. 2012; Aravena et al. 2014; Dessauges-Zavadsky et al. 2017; Brisbin et al. 2019; Sharon et al. 2019; Henríquez-Brocal et al. 2022; Klitsch et al. 2022), and show that while general trends exist in different galaxy populations, the CO ladder of every galaxy is

This indicates that it is necessary to understand how CO emission and excitation vary within galaxies and how they relate to other physical properties in order to correctly interpret H<sub>2</sub> masses derived from high-J transitions. This requires resolved studies of CO line ratios; however, observational limitations at high z make this challenging. To address this, we present a sample of nine galaxies drawn from the DYnamics of Newly Assembled Massive Objects (DYNAMO; Green et al. 2014) observed by ALMA in CO(3-2) and CO(4-3) on  $\sim$ 1–2 kpc scales. DYNAMO galaxies are nearby ( $z \sim 0.1$ ) objects with high gas fractions, high star formation rates, and widespread turbulence, consistent with known properties of high-z main-sequence galaxies, and many are indeed found to lie on the main sequence of star formation at  $z \sim 1-2$  (Fisher et al. 2019). Their resemblance to high-z systems and proximity allows us to probe the CO excitation in gas-rich, turbulent galaxies at scales that are not yet achievable at  $z \sim 2$  in unlensed systems. Furthermore, theories seek to explain CO line ratios by their local radiation field properties (Lagos et al. 2012; Narayanan & Krumholz 2014; Popping et al. 2014; Bournaud et al. 2015), and our ALMA observations allow us to compare to model expectations.

This paper is structured as follows: Section 2 describes our observations, data reduction, and methods; Sections 3 and 4 describe and discuss our results, and finally we conclude in Section 5. Throughout this work, we assume a  $\Lambda$ CDM cosmology with  $H_0 = 69.6$  km s<sup>-1</sup>,  $\Omega_m = 0.286$ , and

 $\Omega_{\Lambda} = 0.714$  (Bennett et al. 2014), and a Kroupa initial mass function (IMF; Kroupa 2001).

#### 2. Observations and Data Reduction

The DYNAMO sample of galaxies was first defined by Green et al. (2014), who selected galaxies from the Max Planck for Astrophysics and Johns Hopkins University Value Added Catalog of the Sloan Digital Sky Survey DR4 (SDSS; Adelman-McCarthy et al. 2006) based on their redshift and  ${
m H}{lpha}$  emission. The sample consists of 67 galaxies, half of which have  $L_{{
m H}{lpha}} > 10^{42}$  erg s<sup>-1</sup> in the 3" diameter SDSS fiber, lying in two redshift windows centered at  $z \sim 0.075$  and  $z \sim 0.13$ . Their stellar masses range from  $10^9$  to  $10^{11}$   $M_{\odot}$  and their SFRs from  $\sim$ 0.1 to 100  $M_{\odot}$  yr<sup>-1</sup>, while their metallicities are similar to the solar metallicity (Tremonti et al. 2004). Employing integralfield spectroscopy of  $H\alpha$ , Green et al. (2014) derived rotation curves and found high ionized-gas velocity dispersions with a mean of  $\sim 50 \,\mathrm{km \, s^{-1}}$ , and gas fractions as high as  $f_{\rm gas} \sim 0.8$  ( $f_{\rm gas} \equiv M_{\rm gas}/(M_{\rm gas}+M_*)$ ;  $M_{\rm gas} = M_{\rm HI} + M_{\rm H_2}$ ). Furthermore, they found that DYNAMO galaxies are more "turbulent" than local disks, as parameterized by their ratio of rotation velocity to velocity dispersion  $(V/\sigma)$ . These properties make DYNAMO galaxies promising candidates for local analogues of high-redshift, star-forming galaxies.

Here, we consider a subset of nine DYNAMO galaxies that have robustly been identified as consistently more similar to  $z \sim 1$ –2 star-forming systems: DYNAMO C13-1, C22-2, D13-5, D15-3, G04-1, G08-5, G14-1, G20-2, and SDSS J013527.10-103938.6 (hereafter SDSS 013527-1039). This builds on a multiwavelength campaign to investigate the nature of star formation at high redshift (Bassett et al. 2014; Fisher et al. 2014; Obreschkow et al. 2015; Fisher et al. 2017a, 2017b; Bassett et al. 2017; White et al. 2017; Girard et al. 2021; Lenkić et al. 2021; Ambachew et al. 2022; White et al. 2022). All galaxies in our sample are classified as rotating disks based on their H $\alpha$  kinematics. Galaxies C22-2, G04-1, G14-1, and G20-2 are furthermore classified as "compact" rotating disks, because their SDSS r-band exponential scale lengths are smaller than 3 kpc. For these, poorer resolution results in less reliable kinematic classifications (Green et al. 2014).

All galaxies in our sample have CO(1-0) observations from either the PdBI or NOEMA, from which molecular gas fractions  $(M_{\rm H_2}/(M_{\rm H_2}+M_*))$  of  $f_{\rm gas}\sim 20\%$ –30% and molecular gas depletion times of  $t_{\rm dep} \sim 0.5$  Gyr are inferred (Fisher et al. 2014; White et al. 2017; Fisher et al. 2019). These highmolecular-gas fractions are consistent with those of  $z \sim 1-2$ main-sequence star-forming galaxies (Daddi et al. 2010; Tacconi et al. 2010, 2013; Genzel et al. 2015; Tacconi et al. 2020). Similarly, subsequent studies of the gas kinematics in these galaxies consistently show that they do indeed have high ionized-gas velocity dispersions (Bassett et al. 2014; Oliva-Altamirano et al. 2018; Girard et al. 2021), similar to mainsequence galaxies at  $z \sim 1-2$  (Förster Schreiber et al. 2006; Übler et al. 2019). In addition, Fisher et al. (2017b) and White et al. (2017) both showed that these DYNAMO galaxies are consistent with marginally stable disks (Toomre  $Q \sim 1$ ). DYNAMO galaxies also conform to established definitions of clumpy galaxies (Fisher et al. 2017b) at high redshift (e.g., Cosmic Assembly Near-infrared Deep Extragalactic Legacy Survey; Guo et al. 2015). Finally, their clumps are arranged within their host disks such that the redder clumps are

Table 1
CO Data Cube Parameters

CO Trans.	Beam F	WHM	rms Noise	CASA Cal.	
	(arcsec) (kpc)		(mK)	C. ISH Cui.	
DYNAMO C13-1					
3 - 2	1.07	1.60	11.5	v5.1.1-5	
DYNAMO C22-2					
3 - 2	1.07	1.46	16.0	v5.1.1-5	
4 - 3	0.81	1.11	12.5	v5.1.1-5	
DYNAMO D13-5					
3 - 2	1.10	1.58	8.2	v5.1.1-5	
4 - 3	0.79	1.14	12.1	v5.1.1-5	
DYNAMO D15-3					
4 - 3	0.96	1.24	10.8	v5.1.1-5	
DYNAMO G04-1					
3 - 2	0.42	0.98	29.1	v5.6.1-8	
4 - 3	0.84	1.96	21.5	v5.1.1-5	
DYNAMO G08-5					
3 - 2	0.40	0.95	32.4	v5.6.1-8	
DYNAMO G14-1 3 – 2	0.43	1.02	3.3	v5.6.1-8	
4 - 3	0.85	2.01	6.3	v5.1.1-5	
DYNAMO G20-2					
3 - 2	1.23	3.08	3.7	v5.1.1-5	
4 - 3	0.86	2.15	4.8	v5.1.1-5	
SDSS 013527-1039					
3 - 2	1.23	2.81	5.2	v5.1.1-5	
4 - 3	0.86	1.97	4.5	v5.1.1-5	

preferentially more centrally located than the bluer ones (Lenkić et al. 2021; White et al. 2022), which has also been observed in  $z \sim 1$ –2 clumpy galaxies (Förster Schreiber et al. 2011; Soto et al. 2017; Guo et al. 2018).

# 2.1. ALMA CO Observations

We make use of the CO(3-2) and CO(4-3) observations of nine DYNAMO galaxies with ALMA, associated with project code 2017.1.00239.S (PI: D. B. Fisher). Observations were taken in Band 7 (275-373 GHz) and Band 8 (385-500 GHz) between 2018 June 1 and 2018 July 10. The spectral windows were configured with bandwidths of 2.00 GHz and channel widths of 15.625 MHz (128 channels). In addition, we also make use of higher-resolution CO(3-2) ALMA observations of three DYNAMO galaxies (G04-1, G08-5, and G14-1) associated with project code 2019.1.00447.S (PI: R. Herrera-Camus). These observations were taken in Band 7 between 2019 October 9 and 2019 October 10. The spectral windows were configured with bandwidths of 1.875 GHz and channel widths of 7.8125 MHz (240 channels). The data associated with both projects were presented in Girard et al. (2021).

The visibilities were calibrated and flagged by the observatory with the Common Astronomy Software Application (CASA; McMullin et al. 2007) pipeline versions listed in the fifth column of Table 1. After calibrating the visibilities, we imaged each observation using tclean in CASA version 6.1.0.188 with the parameters deconvolver=''hogbom,'' weighting=''briggs,'' robust=0.5, usemask=''auto-multi-thresh,'' and restfreq set to the redshifted frequency of

the observed CO line. We cleaned the data until the residuals were consistent with the rms noise levels that are listed in the fourth column of Table 1. To derive these thresholds, we consider data cubes with just a shallow clean, mask the emission (see below), and calculate the standard deviation of the masked cubes, i.e., nonline channels. These values are listed in column four of Table 1, and we reclean the data cubes to that rms level. For visualization purposes and ease of comparison to the H $\alpha$  maps, we convolve the final cubes to a circular beam, listed in the second (angular size) and third (physical size) columns of Table 1, with the CASA imsmooth function. At the redshifts of DYNAMO galaxies in our sample, the beam sizes correspond to physical scales of  $\sim$ 1–2 kpc. Finally, we export all data cubes with the spectral axis in units of velocity, in the local standard of rest frame, adopting the radio convention. We present channel maps of CO(3-2) for DYNAMO G04-1 in Figure 1 to show an example of the final data, with the circularized beam shown at the bottom left corner of each panel. The complete figure set (14 images) is available in the online journal.

We produce moment-zero maps (integrated intensity) by first masking each cleaned data cube along both the spatial and spectral axes. To produce our masks, we first smooth each cleaned data cube to twice the circularized beam FWHM. We then compute the rms of the data cube and mask all pixels that are below  $3\times$  the cube rms. For the remaining pixels, we compute the integrated intensity over the channels that are not masked out. We do this for both the CO(3-2) and CO(4-3) observations. Figure 2 presents these moment-zero maps in the two rightmost panels.

Finally, for the goal of calculating CO(4-3)/CO(3-2)line ratios, we match the pixel scale and resolution of all 2017 CO(4-3) observations to the pixel scale and resolution of the 2017 CO(3-2) observations, where data for both transitions are available. Similarly, we match the pixel scale and resolution of the 2019 CO(3-2) observations, where available, to the 2017 CO(4 -3) observations. We match the pixel scales using the CASA function imregrid, while to match the resolution, we use the CASA imsmooth tool to convolve the higher-resolution data with a Gaussian kernel to produce the lower-resolution Gaussian beam. We note that these transformations are done on the cleaned data cubes with the original, noncircular beams, to ensure we are not introducing errors or artifacts in the data. Finally, we apply the masking of the CO(3-2) observations to the CO(4-3) to produce matching integrated intensity maps. This ensures that the intensities we derive for both lines are integrated over the same velocity ranges and regions.

# 2.2. HST H\alpha Observations

In addition to the ALMA observations of CO, we make use of Hubble Space Telescope (HST) observations of H $\alpha$  (PID 12977; P.I.: I. Damjanov) as a tracer of the star formation rate (leftmost panel of Figure 2). Observations were taken with the Wide Field Camera on the Advanced Camera for Surveys (WFC/ACS) using the FR716N and FR728N narrowband filters and were processed with the standard HST pipeline. Continuum observations with the FR647M filter were also taken and used to create continuum-subtracted H $\alpha$  maps (for details, see Section 3.2 of Fisher et al. (2017a)). The final H $\alpha$  maps have a pixel scale of  $\sim$ 0."05 and a resolution corresponding to physical scales of  $\sim$ 50–200 pc (Fisher et al. 2017a).

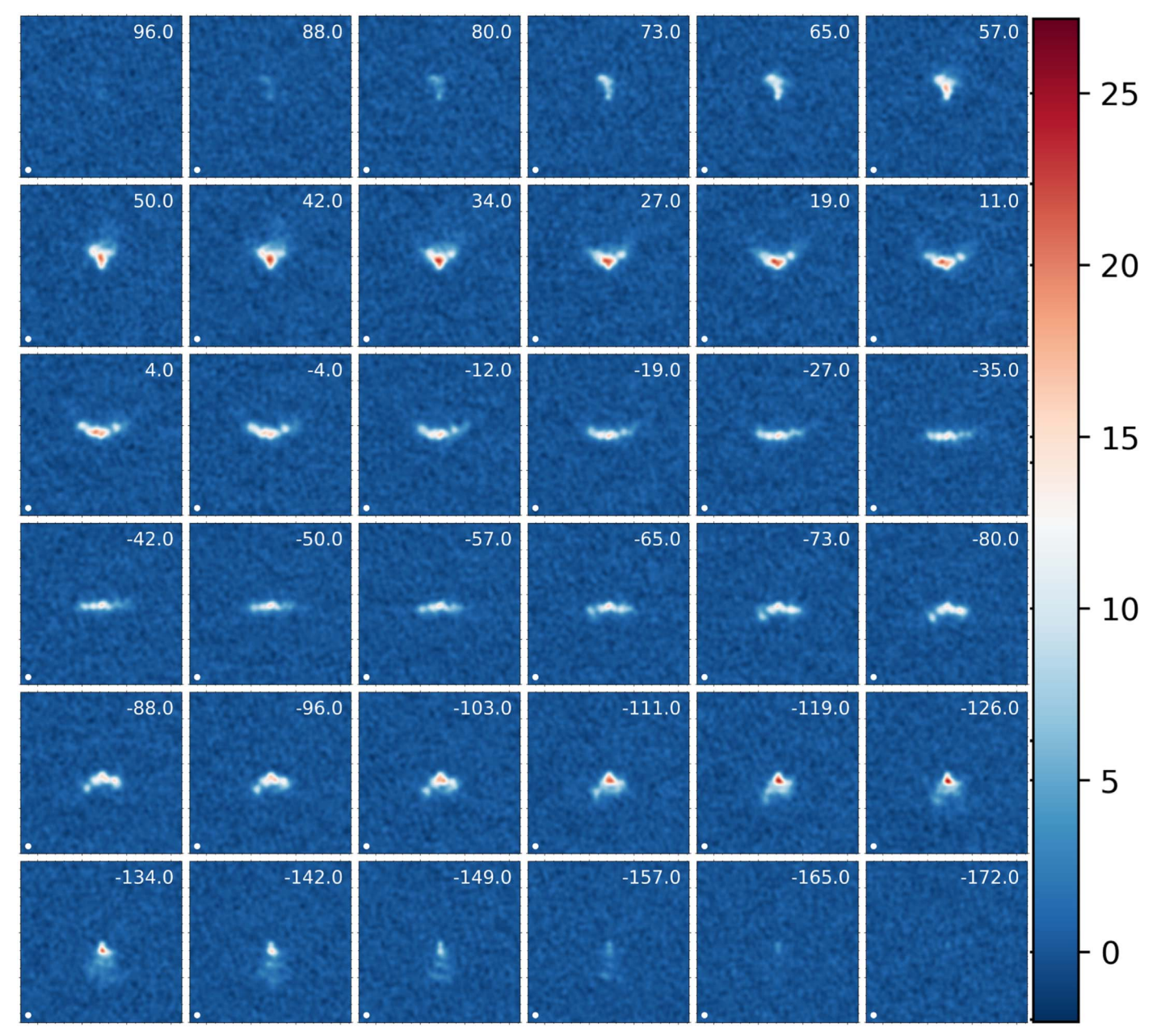


Figure 1. Channel maps of CO(3-2) in brightness units of Jy beam<sup>-1</sup> for the galaxy DYNAMO G04-1. Each panel is centered at  $04^{\rm h}12^{\rm m}19^{\rm s}.713$ ,  $-05^{\rm d}54^{\rm m}48^{\rm s}.62$ , and is  $10\rlap.{''}8 \times 10\rlap.{''}8$  in size. The velocity range is -172-96 km s<sup>-1</sup> in steps of  $\sim 8$  km s<sup>-1</sup>, as indicated at the top right corners. The circularized beam is shown in white at the bottom left corner of each panel. The complete figure set (14 images) is available in the online journal. (The complete figure set (14 images) is available.)

Our ability to make resolved measurements in these DYNAMO galaxies is limited by the resolution of the ALMA data; therefore, we match the pixel scale and resolution of the H $\alpha$  observations to that of the CO(3–2), where available, and CO(4–3) otherwise. To achieve this, we convolve each H $\alpha$  observation with a two-dimensional Gaussian function whose FWHM is equal to the circularized beam of the corresponding ALMA observation. Then, we reproject and regrid the H $\alpha$  observations to match the WCS information and pixel scale of the CO observations using the PYTHON ASTROPY package reproject, <sup>10</sup> noting that the reproject functions assume that input images have surface brightness units.

## 2.3. SOFIA FIFI-LS and HAWC+ Observations

Finally, we make use of observations from the Stratospheric Observatory for Infrared Astronomy (SOFIA) of DYNAMO galaxies taken by the Field-Imaging Far-Infrared Line Spectrometer (FIFI-LS; Colditz et al. 2018; Fischer et al. 2018) and High-resolution Airborne Wideband Camera Plus (HAWC+; Harper et al. 2018) instruments (PLAN ID 08\_0238 and 09\_158; P.I.: L. Lenkić) as part of Cycles 8 and 9. The FIFI-LS is an integral-field spectrometer with two channels observing simultaneously from 50 to 125  $\mu$ m (blue channel) and 105–200  $\mu$ m (red channel). The FIFI-LS observations targeted the [CII] 158  $\mu$ m fine-structure emission line in the red channel and the [OIII] 88  $\mu$ m fine-structure line (or [OI] at 63  $\mu$ m

<sup>10</sup> https://reproject.readthedocs.io/en/stable/index.html

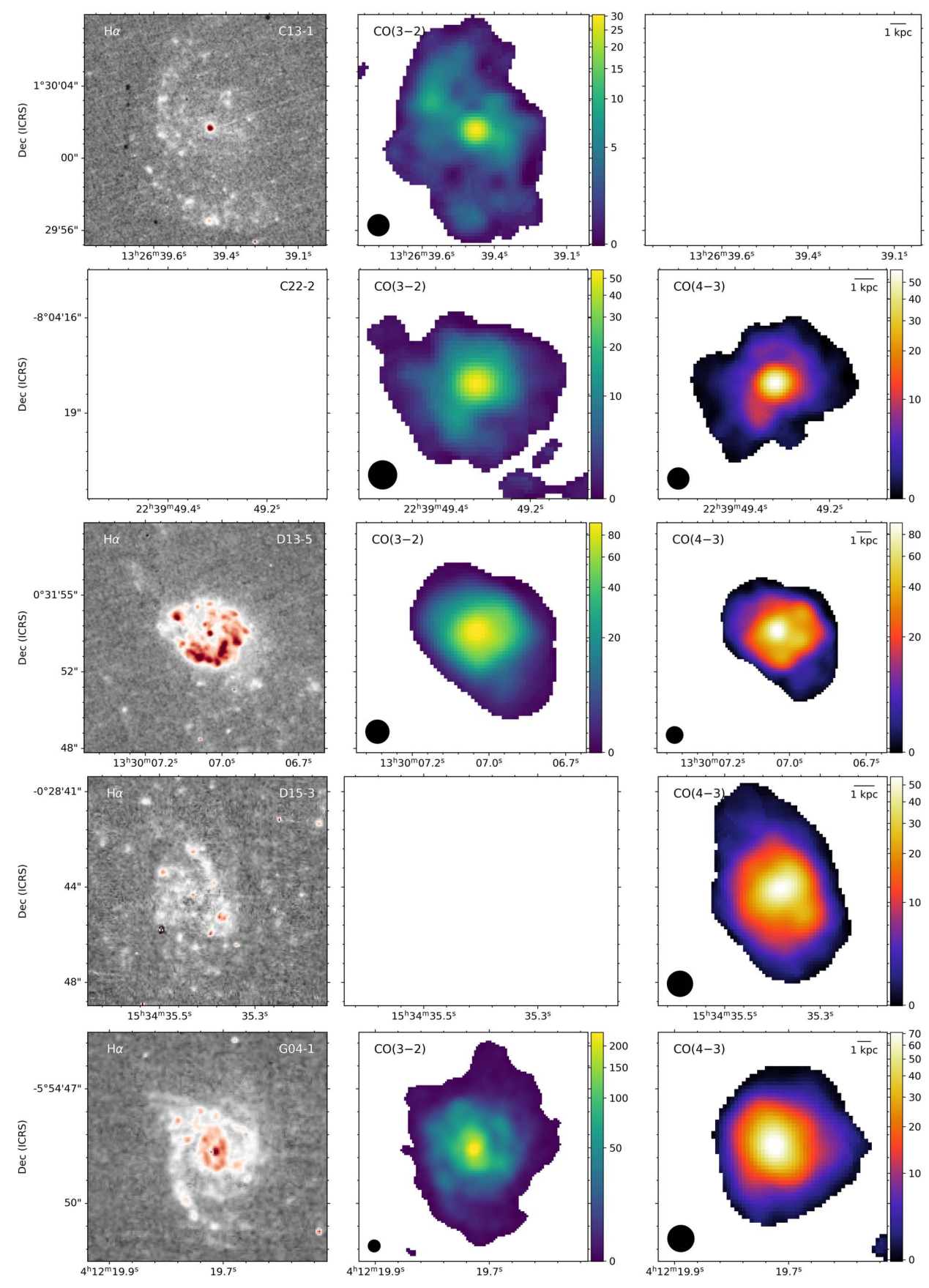


Figure 2. Summary of data sets analyzed in this work for each galaxy in our sample, as indicated at the top right corners of the leftmost panels: HST H $\alpha$  (left), CO(3-2) integrated intensity (middle), CO(4-3) integrated intensity (right; both in units of K km s<sup>-1</sup>). We show all images using an arcsinh stretch. The ALMA CO beam sizes are at the bottom left corners of the middle and rightmost panels, while 1 kpc scale bars are shown at the top right corners of the rightmost panels. Empty panels indicate that data are absent for the given galaxy.

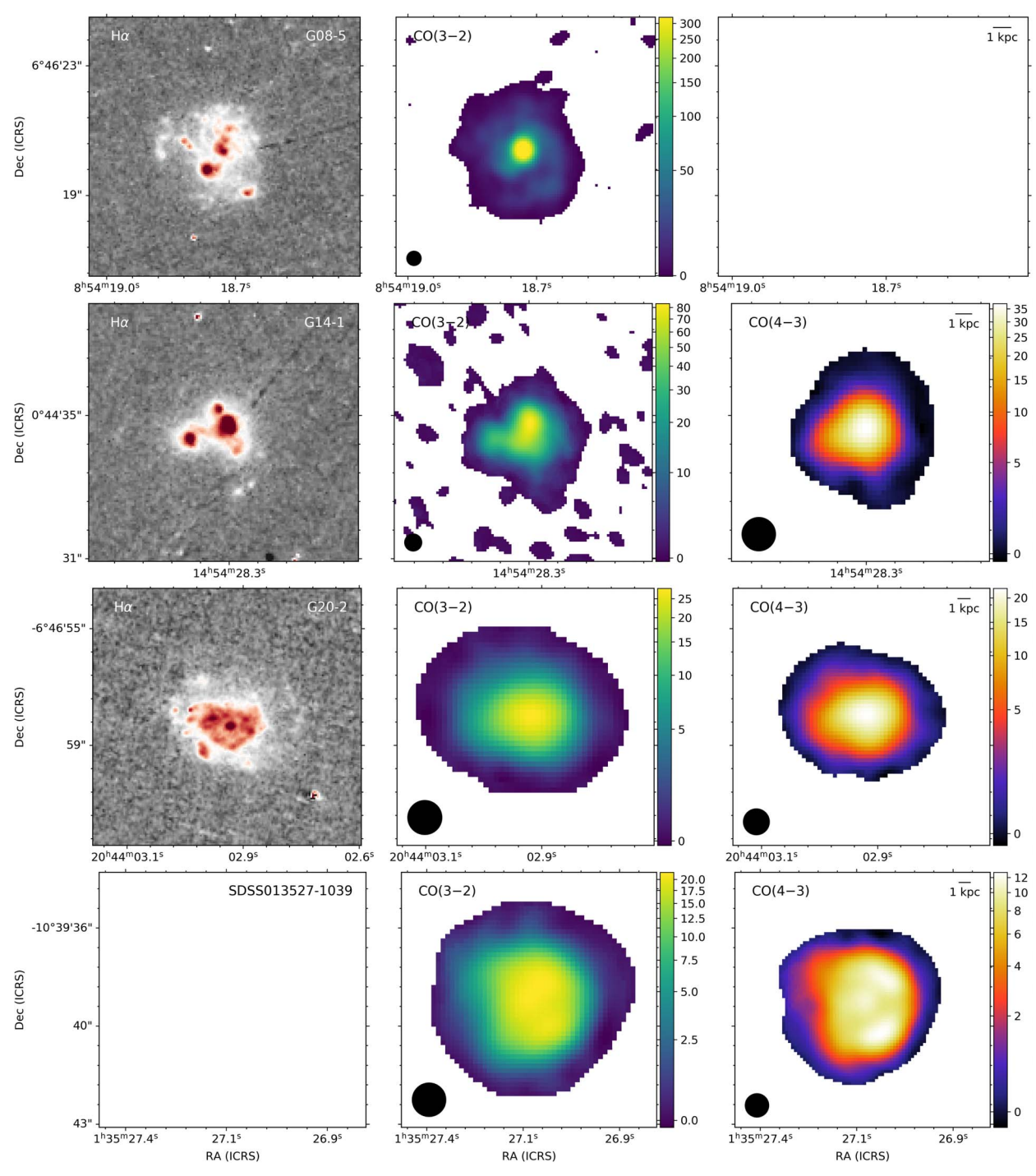


Figure 2. (Continued.)

depending on atmospheric transmission) in the blue channel for six galaxies (DYNAMO B08-3, D10-4, D14-1, D15-3, F08-2, F09-1, and F12-4) at  $15\rlap.{''}6$  resolution. These data cover a  $1\times1$  arcmin² field of view (FOV) in the red channel and a  $30\times30$  arcsec² FOV in the blue channel. FIFI-LS observations were taken on six nights in 2021 April in the nod-match-chop mode, and were reduced using the FIFI-LS pipeline  $^{11}$  (Vacca et al. 2020). The data reduction steps include ramp fitting and flagging bad pixels, subtracting the chops, wavelength, and spatial calibration, flat-field correction, atmospheric

transmission correction using the ATRAN models (Lord 1992), flux calibration, and finally resampling to a regular grid to produce the final data cubes. The observations resulted in [CII] detections for all galaxies in the sample, and an [OIII] detection in DYNAMO F08-2 (see Figure 8 in Appendix A).

The HAWC+ instrument is an FIR camera and imaging polarimeter with a wavelength coverage of  $50-240~\mu m$ . The HAWC+ observations targeted four galaxies (DYNAMO D14-1, D15-3, F08-2, and F12-4) in bands C, D, and E. These data provide measurements of the 89, 155, and 216  $\mu m$  fluxes at a resolution of 7.8, 14", and 19", respectively. Observations were taken on three nights in 2021 May and one night in 2021

<sup>11</sup> FIFI-LS Redux User's Manual

November in the on-the-fly mapping mode with a Lissajous scan pattern, and were reduced using the HAWC+ pipeline. <sup>12</sup> The observations resulted in detections for all galaxies in the sample (see Figure 9 in Appendix A).

The typical sizes of galaxies in this sample are ~4", and our sources are thus point sources for both the FIFI-LS and HAWC + observations. Appendix A presents the HAWC+ observations in Figure 9 and the FIFI-LS integrated intensity maps in Figure 8. While DYNAMO D13-5 is the only galaxy that overlaps with our ALMA sample, we make use of all SOFIA observations described here to measure the spectral energy distributions (SEDs) of DYNAMO galaxies, and place the measured dust temperatures within the global context of the line ratio measurements we will present. We also make use of these observations to measure the [CII] luminosity and measure the [CII]-to-total far-infrared luminosity ratios.

#### 2.4. Resolved Measurements

This work aims to investigate the CO(4-3)/CO(3-2) properties of DYNAMO galaxies resolved on a 1–2 kpc scale, and to relate this line ratio to the star formation rate surface density ( $\Sigma_{SFR}$ ) on the same scale. Thus, we describe here our method for extracting these measurements from the data. For each of our resolution and WCS matched ALMA and HST data sets (excluding SOFIA observations because they are unresolved), we define two sets of "grids" of circular, beam-sized apertures: one that is centered on the galaxy, and a second that is offset from the center by  $0.5 \times$  the beam FWHM in both the x and y directions. This is to ensure that we cover the gaps of the first grid and results in measurements that are not entirely independent. Within each aperture, we measure the median brightness temperatures of both the CO(3-2) and CO(4-3) lines from the integrated intensity maps and take their ratio.

We measure the SFR surface density from our CO-matched  $H\alpha$  observations. We perform aperture photometry within each ALMA beam-sized aperture in our two grids, described above, to obtain the  $H\alpha$  flux (in electrons per second). We convert these fluxes to units of erg s<sup>-1</sup> cm<sup>-2</sup>  $\mathring{A}^{-1}$ , apply a correction for extinction by relating  $A_V$  to  $A_{H\alpha}$  assuming the Cardelli et al. (1989) extinction law and the  $A_V$  measurements from Lenkić et al. (2021). Bassett et al. (2017) used Pa $\alpha$  observations from the OH-Suppressing Infrared Integral-field Spectrograph instrument at Keck to make resolved extinction measurements in four DYNAMO galaxies. Their results show up to a magnitude difference in  $A_{H\alpha}$ ; however, strong variation in the adaptive optics point-spread function introduces significant systematic uncertainties in measuring the Pa $\alpha$  flux. Furthermore, Bassett et al. (2017) also found that the average  $A_{H\alpha}$  in clump and nonclump regions are, within the uncertainties, consistent with one another (see their Table 3). This is consistent with the results of Lenkić et al. (2021), who found that within a given DYNAMO galaxy, the extinction-sensitive color they measure shows little variation between clumps, and the clump colors are consistent with their host disks (see their Figures 5 and 8). For these reasons, we choose to adopt a single  $A_V$  value for each galaxy. Finally, we calculate H $\alpha$  luminosities and convert them to SFRs using the Hao et al. (2011) calibration for a Kroupa IMF, constant star formation history, and age of 100 Myr (see their Table 2):

SFR 
$$[M_{\odot} \text{ yr}^{-1}] = 5.53 \times 10^{-42} \times L_{\text{H}\alpha} [\text{erg s}^{-1}].$$
 (1)

#### 3. Results

3.1. 
$$CO(4-3)/CO(3-2)$$
 Line Ratios

In Section 2.1, we describe our process for matching our CO(4-3) and CO(3-2) observations and deriving integrated intensity maps. We adopt brightness temperature units, thus our integrated intensity maps have units of K km s<sup>-1</sup>. To visually determine how this line ratio varies across each galaxy disk, if at all, we simply divide our CO(4-3) integrated intensity map by that of the CO(3-2). This is what we present in Figure 3, where the color scale indicates the ratio variations across each galaxy disk for which both line transitions were observed, and where the line ratio has  $S/N \ge 3$ , and the black contours correspond to  $H\alpha$  emission in the pixel scale and resolutionmatched HST observations. The contours span  $1-10\sigma$  in increments of  $1\sigma$ , where we take  $\sigma$  to correspond to the rms of each HST observation calculated in galaxy emission-free regions. We note that there are no HST  $H\alpha$  observations for DYNAMO C22-2 and SDSS 013527-1039. We derive uncertainties for the integrated intensity maps  $(\sigma_{J \to J-1})$  by summing in quadrature the rms of every channel over which we integrate, excluding line emission from the rms calculation, and multiplying by the channel width:

$$\sigma_{J \to J-1} = \Delta v \sqrt{\sum_{i}^{N} (\text{rms}_{i})^{2}},$$
 (2)

where  $\Delta v$  is the channel width, rms<sub>i</sub> is the rms of the i<sup>th</sup> channel, and N is the number of channels over which the emission is integrated. To obtain the final uncertainty on the line ratio per pixel, we propagate the integrated intensity uncertainties by taking:

$$\sigma_{lr} = \frac{\text{CO}(4-3)}{\text{CO}(3-2)} \sqrt{\left(\frac{\sigma_{43}}{\text{CO}(4-3)}\right)^2 + \left(\frac{\sigma_{32}}{\text{CO}(3-2)}\right)^2}, \quad (3)$$

which results in line ratio uncertainty maps.

From Figure 3, we see that the line ratio for galaxies in our sample vary mildly across the disks, with typical values ranging from  $R_{43} \sim 0.4$ –0.7. However, galaxy DYNAMO G14-1 shows a strong gradient in the line ratio, with values approaching unity. The H $\alpha$  image of G14-1 in Figure 2 shows two bright clumps with a fainter "stream" connecting the two. The H $\alpha$  contours we overplot in Figure 3 show that these two bright features with the connecting filament coincide with the elevated line ratio values and the strong gradient. This may be indicative of an interaction taking place; however, the  $H\alpha$ kinematics of G14-1 show a rotating disk and no complex kinematics (Green et al. 2014). Overall, the line ratio maps we show in Figure 3 suggest a potential central enhancement in  $R_{43}$ . Such a central enhancement has been observed in the Milky Way and other nearby star-forming galaxies for CO(2-1)/ CO(1-0) (see, e.g., Sakamoto et al. 1997; Sawada et al. 2001; Leroy et al. 2009, 2013; den Brok et al. 2021). To verify this, we separate pixels that are located within the central kiloparsec of each galaxy from pixels that lie outside this region, and compare the median line ratios. Indeed, we find enhanced CO(4-3)/ CO(3-2) values in the central kiloparsec of all galaxies in Figure 3, except for G04-1 and G14-1, on the order of  $\sim$ 10%

<sup>12</sup> HAWC+ DRP User's Manual

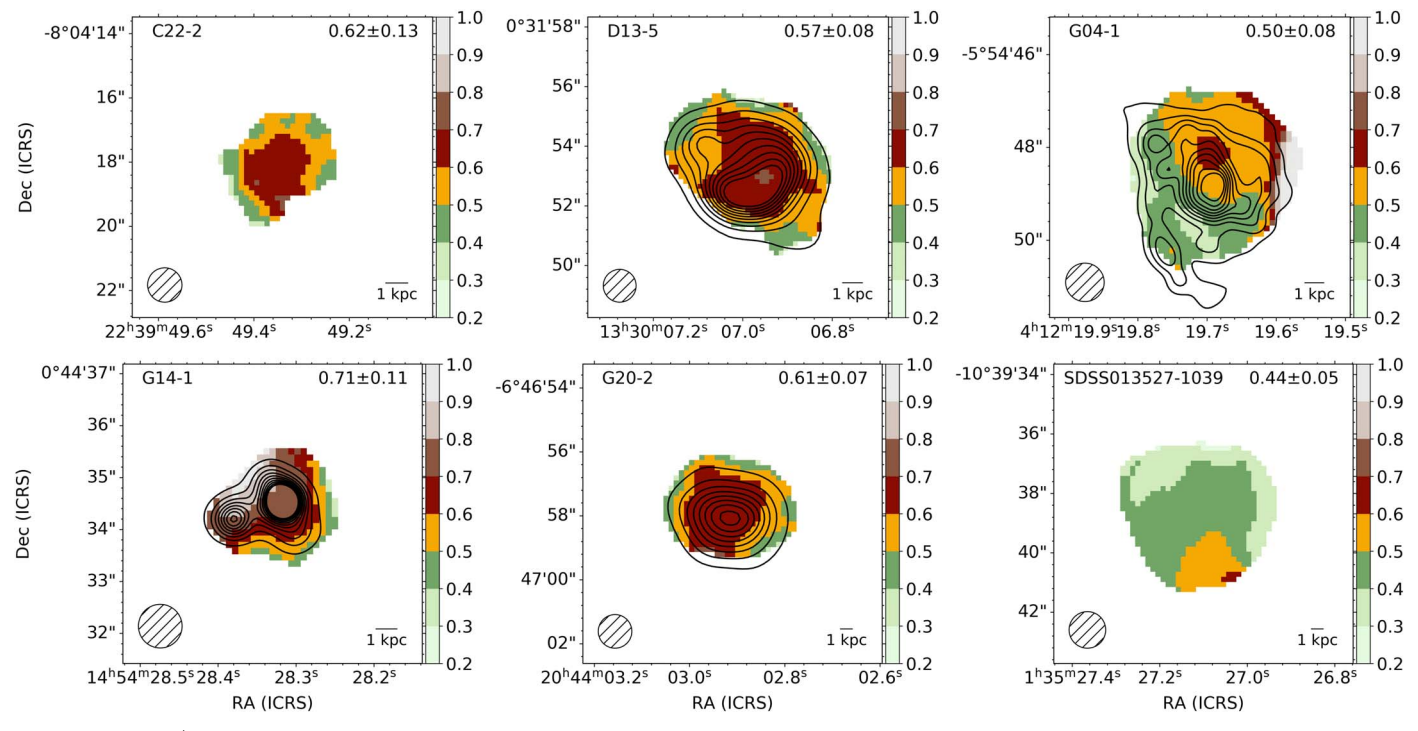


Figure 3. CO(4-3)/CO(3-2) line ratios (in brightness temperature units) measured from the pixel scale and resolution-matched integrated intensity maps, integrated over the same velocity ranges. These maps show CO(4-3)/CO(3-2) only in regions where the line ratio has  $S/N \geqslant 3$ . The black contours correspond to  $H\alpha$  emission, where available, ranging from 1 to  $10\sigma$  in increments of  $1\sigma$ . The galaxy name is indicated at the top left corner of each panel, the median line ratios and their associated uncertainties are at the top right corners, and the black hatched circles at the bottom left corners indicate the circularized beam sizes. Finally, we show a 1 kpc scale bar at the bottom right corners. We see that galaxies generally have mildly varying line ratios within the regions where the uncertainties do not dominate, and that they lie typically around 0.4–0.7, with the exception of DYNAMO G14-1, which has a stronger varying line ratio.

(see Table 2). Finally, Figure 3 shows in particular for galaxy G04-1, variations in  $R_{43}$  between the spiral arm and interarm region, a trend also observed for CO(2-1)/CO(1-0) in M51 (Koda et al. 2012).

Next, we perform  $\sim$ 1–2 kpc sized sightline measurements of the line ratio across the disk of each galaxy, as described in Section 2.4. To characterize the typical line ratio we measure across the sample and the magnitude of the spread. To this end, we construct a global probability density function (PDF) by modeling each beam-averaged line ratio measurement with a kernel density estimate (KDE). We construct the individual KDEs by modeling each beam-averaged line ratio measurement as a one-dimensional Gaussian with a centroid corresponding to the measured line ratio and with width equal to the line ratio uncertainty. The area of each Gaussian is normalized to unity; then we sum all Gaussians to produce a final global PDF (see for example Section 4 and Figure 5 of Levy et al. (2018)). This is what we show in Figure 4. From this, we find that the median line ratio and 68% confidence interval for DYNAMO galaxies are:  $R_{43} = 0.54^{+0.16}_{-0.15}$ . These values are taken at the 15.9, 50, and 84.1 percentiles of the cumulative distribution function of the PDF.

For comparison, we compile estimates of the CO(4-3) to CO(3-2) line ratio from the literature and include these in Figure 4. We describe our derivation of all line ratios compiled from the literature in Appendix B, and we summarize them along with the median line ratios we measure for each DYNAMO galaxy individually, and the median line ratio for the entire DYNAMO sample studied here in Table 2.

This comparison reveals that the CO(4-3)/CO(3-2) line ratio of non-ULIRGs from Kamenetzky et al. (2016; local

galaxies with  $L_{\rm FIR} \leqslant 6 \times 10^{10} \, L_{\odot}$ ) is much lower and incompatible with what we find in our DYNAMO sample. In contrast, the U/LIRG line ratio estimate from Kamenetzky et al. (2016) for  $L_{\rm FIR} = 10^{11} L_{\odot}$  is in much better agreement with what we find across the DYNAMO sample. Likewise, the CO(4-3)/CO(3-2) line ratios measured in main-sequence galaxies at  $z \sim 1-2$  (Daddi et al. 2015; Boogaard et al. 2020; Henríquez-Brocal et al. 2022) are, within the uncertainties, consistent with DYNAMO. In particular, the eight star-forming galaxies at z = 1.0-1.6 from the ALMA Spectroscopic Survey (ASPECS; Boogaard et al. 2020), are an especially good match to the  $R_{43}$  we measure across our sample. DYNAMO galaxies lie on the star formation main sequence at  $z \sim 2$  (Fisher et al. 2019) and have gas fractions and velocity dispersions that are more similar to main-sequence galaxies of that epoch than local ones. Therefore, this result is consistent with lines of evidence that indicate DYNAMO galaxies are local analogues of high-z main-sequence systems. ULIRG samples (Rosenberg et al. 2015) have much larger line ratios than we observe in DYNAMO, and this too is consistent with previous observations. Using Herschel Photodetector Array Camera and Spectrometer (PACS) and Spectral and Photometric Imaging Receiver (SPIRE) observations of five DYNAMO galaxies, White et al. (2017) found that, despite their large FIR luminosities,  $L_{\rm FIR} > 10^{11} L_{\odot}$ , these galaxies have much lower dust temperatures (~30 K) than ULIRGs. Therefore, unlike ULIRGs, the star formation in DYNAMO galaxies is more distributed throughout the disks; thus, colder dust temperatures would be expected and likewise lower CO(4-3)/CO(3-2) line ratios.

Object(s)	Line Ratio	Reference
C22-2	$0.62 \pm 0.13$	This work
C22-2 (≤1 kpc)	$0.60 \pm 0.10$	This work
C22-2 (>1 kpc)	$0.52 \pm 0.08$	This work
D13-5	$0.57 \pm 0.08$	This work
D13-5 (≤1 kpc)	$0.60 \pm 0.08$	This work
D13-5 (>1 kpc)	$0.56 \pm 0.09$	This work
G04-1	$0.50 \pm 0.08$	This work
G04-1 ( $\leq$ 1 kpc)	$0.48 \pm 0.20$	This work
G04-1 (.1 kpc)	$0.52 \pm 0.16$	This work
G14-1	$0.71 \pm 0.11$	This work
G14-1 (≤1 kpc)	$0.70 \pm 0.13$	This work
G14-1 (>1 kpc)	$0.71 \pm 0.16$	This work
G20-2	$0.61 \pm 0.07$	This work
G20-2 (≤1 kpc)	$0.62 \pm 0.10$	This work
G20-2 (>1 kpc)	$0.57 \pm 0.10$	This work
SDSS J013527.10-103938.6	$0.44 \pm 0.05$	This work
SDSS J013527.10-103938.6 (≤1 kpc)	$0.46 \pm 0.06$	This work
SDSS J013527.10-103938.6 (>1 kpc)	$0.42\pm0.06$	This work
DYNAMO all	$0.54^{+0.16}_{-0.15}$	This work
z = 1.5 MS Galaxies	$0.74 \pm 0.26$	D15
ASPECS $z = 1.0-1.6$ SFGs	$0.52 \pm 0.16$	B20
G1700-MD94 one component	$0.92\pm0.18$	HB22
G1700-MD94 two component	$0.77 \pm 0.15$	HB22
non-U/LIRGs ( $L_{\rm FIR} = 10^{10} L_{\odot}$ )	$0.25\pm0.05$	K16
LIRGs $(L_{\rm FIR} = 10^{11} L_{\odot})$	$0.51 \pm 0.10$	K16
LIRGs	$1.23\pm0.38$	P12
ULIRGs low CO excitation	1.08	R15
ULIRGs mid CO excitation	0.70	R15
ULIRGs high CO excitation	1.02	R15

## 3.2. Relating High-J CO to CO(1-0)

We make use of existing CO(1-0) measurements from the PdBI and NOEMA (angular resolution  $\sim 5''-10''$ ; Fisher et al. 2014; White et al. 2017; Fisher et al. 2019) to derive the CO(4-3)/CO(1-0) and CO(3-2)/CO(1-0) line ratios across our sample. We measure the total CO(4-3) and CO(3-2) fluxes by summing all pixels with  $S/N \geqslant 3$  in our integrated intensity moment maps and then scaling by the number of pixels per beam. We then convert the total fluxes to luminosities (L'; K km s<sup>-1</sup> pc<sup>2</sup>) using Equation (3) in Solomon et al. (1997). We present these results in Table 3.

We find line ratio values across our sample that range from  $R_{31} \sim 0.4-0.8$ , with a mean (median)  $R_{31} = 0.56 (0.55)$  and  $R_{41} \sim 0.2$ –0.4, with a mean (median)  $R_{41} = 0.27$  (0.28). Our  $R_{31}$  result is consistent with multiple studies of CO excitation in  $z \sim 1-3$  star-forming galaxies: Daddi et al. (2015) found that the brightness temperature line ratio of CO(3-2) to CO(1-0)ranges from  $R_{31} \sim 0.4-0.6$ , with an average  $R_{31} = 0.42 \pm 0.07$ , for their three star-forming BzK  $z \sim 1.5$  galaxies; Dessauges-Zavadsky et al. (2015) found  $R_{31} = 0.57 \pm 0.15$  for five lensed star-forming galaxies (SFR < 40  $M_{\odot}$  yr<sup>-1</sup>) at  $z \sim 1.5$  galaxies; Riechers et al. (2020) found  $R_{31} = 0.84 \pm 0.26$  for six galaxies at  $z \sim 2-3$ ; Birkin et al. (2021) found  $R_{31} = 0.63 \pm 0.12$  for a large sample of SMGs at  $z \sim 1.2$ –4.8; and Harrington et al. (2021) found  $R_{31} = 0.69 \pm 0.12$  for 24 dusty star-forming galaxies at 1 < z < 3. However, we note that Bolatto et al. (2015) found  $R_{31} \sim 1$  for two main-sequence galaxies at  $z \sim 2$ ; however, one of the two galaxies is classified as an

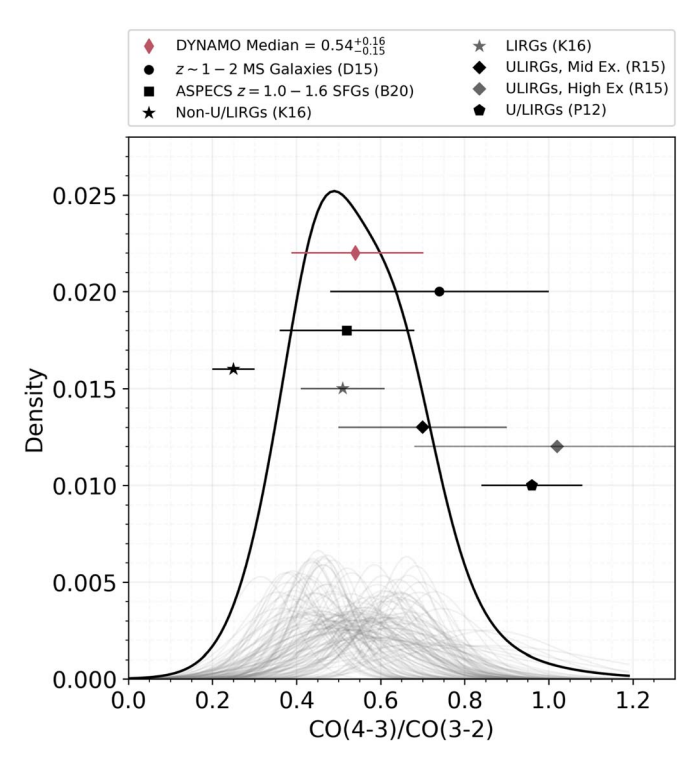


**Figure 4.** Global PDF for the resolved CO(4-3)/CO(3-2) line ratio measurements. We construct the PDF by modeling each line-of-sight  $R_{43}$  measurement (where  $S/N \geqslant 3$ ) as a Gaussian whose width is the line ratio uncertainty. We show these individual Gaussians as light gray lines (not to scale); summing them and normalizing the area of the resulting Gaussian to unity results in the solid black line shown here. From the cumulative distribution function, we infer a median line ratio of  $R_{43}=0.54$ . For comparison, we include estimates from the literature:  $R_{43}=0.74\pm0.26$  for three  $z\sim1.5$  main-sequence star-forming galaxies (black circle; Daddi et al. 2015),  $R_{43}=0.52\pm0.16$  in eight star-forming galaxies at z=1.0-1.6 (black square; Boogaard et al. 2020),  $R_{43}=0.25\pm0.05$ ,  $0.51\pm0.10$  for non-U/LIRGs with  $L_{\rm FIR}=10^{10}~L_{\odot}$  and U/LIRGs with  $L_{\rm FIR}=10^{11}~L_{\odot}$ , respectively (black stars; Kamenetzky et al. 2016),  $R_{43}=0.70$ , 1.02 for mid- and high-excitation ULIRGs, respectively (black diamonds; Rosenberg et al. 2015), and  $R_{43}=0.96\pm0.12$  for LIRGs (black pentagon; Papadopoulos et al. 2012).

AGN, and the other may host a weak AGN. In contrast, Leroy et al. (2022) analyzed the global  $R_{31}$  for nearby normal star-forming galaxies and find a mean (median) of  $R_{31} = 0.30 (0.29)$ , which are lower and inconsistent with the DYNAMO results, but similar to the Milky Way (Fixsen et al. 1999). We illustrate this comparison in Figure 5 where we plot the brightness temperature ratios of DYNAMO galaxies as a function of the upper-J number, along with the ratios of  $z \sim 1-2$ star-forming galaxies (Daddi et al. 2015; Boogaard et al. 2020), nearby star-forming galaxies (Leroy et al. 2022), and the Milky Way inner disk (Fixsen et al. 1999). We can see that the ratios of nearby galaxies and the Milky Way are incompatible with those of DYNAMO. The CO SLED of the ASPECS galaxies and two of the three BzK galaxies are in agreement with DYNAMO, while the third galaxy (referred to as BzK-16000 in Daddi et al. 2015) shows overall lower line ratios. Interestingly, Daddi et al. (2015) describe this galaxy as the most evolved in their sample, with no massive clumps.

# 3.3. DYNAMO SEDs and [CII] Emission

We extract background-subtracted 89, 155, and 216  $\mu m$  fluxes for four DYNAMO galaxies, including D15-3, which overlaps with our ALMA sample, from our HAWC+ SOFIA

Table 3
Galaxy Integrated CO(3-2)/CO(1-0) and CO(4-3)/CO(1-0) Line Ratios and Model Predictions

Galaxy	$L'_{\text{CO}(1-0)}$	$L'_{\text{CO(3-2)}}$	$L'_{\text{CO(4-3)}}$	R <sub>31</sub>	$R_{41}$	R <sub>31</sub>	$R_{41}$	
	2 20(1 0)		$(10^9 \text{ K km s}^{-1} \text{ pc}^2)$		Observed		Predicted	
C13-1	$1.91 \pm 0.05$	$0.47 \pm 0.05$		$0.40 \pm 0.05$			•••	
C22-2	$0.66 \pm 0.05$	$0.47 \pm 0.04$	$0.23 \pm 0.02$	$0.71 \pm 0.08$	$0.35 \pm 0.04$			
D13-5	$2.69 \pm 0.08$	$1.48 \pm 0.03$	$0.87 \pm 0.03$	$0.55 \pm 0.02$	$0.32 \pm 0.01$	0.63	0.39	
D15-3	$3.02 \pm 0.06$		$0.49 \pm 0.02$	•••	$0.16 \pm 0.01$	0.57	0.32	
G04-1	$5.41 \pm 0.39$	$2.90 \pm 0.10$	$1.54 \pm 0.08$	$0.54 \pm 0.04$	$0.28 \pm 0.02$	0.56	0.31	
G08-5	$2.29 \pm 0.26$	$1.83 \pm 0.08$		$0.80 \pm 0.10$		0.57	0.32	
G14-1	$1.59 \pm 0.19$	$0.77 \pm 0.08$	$0.427 \pm 0.001$	$0.48 \pm 0.08$	$0.27 \pm 0.03$	0.56	0.31	
G20-2	$1.68 \pm 0.19$	$0.97 \pm 0.03$	$0.56 \pm 0.03$	$0.58 \pm 0.07$	$0.33 \pm 0.04$	0.61	0.36	
SDSS 013527-1039	$3.45\pm0.16$	$1.48\pm0.05$	$0.65 \pm 0.02$	$0.43\pm0.02$	$0.19 \pm 0.01$	•••		

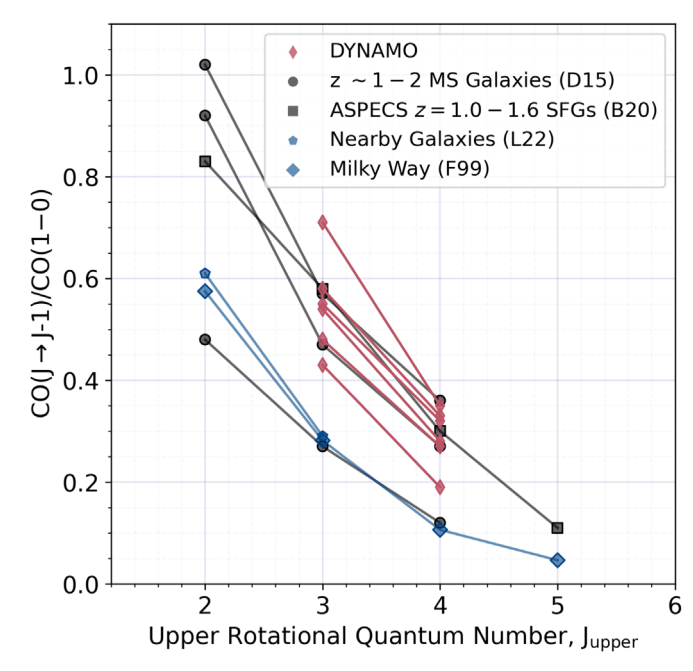


**Figure 5.** CO ladders normalized to CO(1–0) in integrated brightness temperature units, for DYNAMO galaxies (red small diamond),  $z\sim 1$ –2 main-sequence BzK galaxies (black circles; Daddi et al. 2015), z=1.0–1.6 star-forming galaxies from ASPECS (black squares Boogaard et al. 2020) nearby star-forming galaxies (blue pentagons; Leroy et al. 2022), and the Milky Way inner disk (blue large diamonds; Fixsen et al. 1999). DYNAMO line ratios are consistent with  $z\sim 1$ –2 star-forming galaxies, while the nearby star-forming galaxies and the Milky Way show an overall lower CO excitation. One galaxy from the sample of Daddi et al. (2015; BzK-16000) is more consistent with nearby galaxies and the Milky Way than with DYNAMO. BzK-16000 is more evolved and has no massive clumps.

observations using the PHOTUTILS software (Bradley et al. 2021). We define the flux extraction apertures to correspond to the FWHM beam size of each corresponding HAWC+ band, while we define the background annuli to have an inner radius equal to  $5 \times$  beam FWHM and an outer radius of  $7 \times$  beam FWHM (see Figure 9 in Appendix A). We record these flux measurements in Table 4. To fit the SED, we combine the HAWC+ fluxes with Wide-field Infrared Survey Explorer (WISE) measurements at  $22 \mu m$  (which is not contaminated by line emission and traces the warm dust continuum; Cluver et al. 2017), and use the modified blackbody (MBB) SED fitting tool MBB\_EMCEE, <sup>13</sup> described in Riechers et al. (2013) and Dowell et al. (2014). The MBB is

joined to a power law of the form  $\nu^{\alpha}$  at short wavelengths. MBB\_EMCEE fits the dust temperature,  $T_{\rm d}$ , the extinction curve power-law slope,  $\beta$ , the power-law slope of the blue side,  $\alpha$ , the wavelength where the optical depth reaches one,  $\lambda_0$ , and the normalization. We impose a prior on  $\beta$  to constrain it between 1.5 and 2, and leave all other parameters unconstrained. We record the resulting fit parameters and total infrared luminosity (TIR; 8–1000  $\mu$ m) in Table 4.

We present the resulting SEDs in the left panel of Figure 6, where the filled colored data points represent fluxes from the HAWC+ (three longest wavelength data points), open colored data points represent WISE bands (shortest wavelength point) for each of the four galaxies, and the matching colored line represents the SED fit for that galaxy. The dust temperatures derived from these SEDs are shown in the upper left corner. For DYNAMO D14-1 and D15-3, the resulting dust temperatures are  $T_d = 25.94^{+5.10}_{-4.88}$  K and  $T_d = 29.56^{+3.06}_{-2.89}$  K, respectively, consistent with the dust temperature measurements of  $T_d = 28.09 \pm 0.86$  K and  $T_d = 25.64 \pm 0.52$  K from SED fitting of Herschel PACS and SPIRE observations by White et al. (2017).

The SEDs provide us with estimates of the TIR for four out of the seven galaxies in the SOFIA sample. We combine these measurements with the SOFIA FIFI-LS observations to explore the "[CII] deficit": the observed decreasing fraction of [CII] emission with respect to the TIR in increasingly more infrared luminous objects (see, e.g., Malhotra et al. 2001; Brauher et al. 2008; Smith et al. 2017; Herrera-Camus et al. 2018a). For the remaining four galaxies in the SOFIA sample where no HAWC + observations are available, we instead use the SFRs reported in Green et al. (2014) to estimate the TIR and the calibration in Equation (3) of Cluver et al. (2017):

SFR 
$$[M_{\odot} \text{ yr}^{-1}] = 2.8 \times 10^{-44} L_{\text{TIR}} [\text{erg s}^{-1}],$$
 (4)

which is derived from STARBURST99 for solar metallicity, continuous star formation over 100 Myr, and a Kroupa IMF, and assumes that the ultraviolet (UV) component of stellar emission is completely absorbed and reradiated in the infrared (see also Calzetti 2013).

To determine the [CII] luminosities, we produce integrated intensity maps from the FIFI-LS observations (see Figure 8 in Appendix A) and take the peak value within a beam located at the position of each galaxy. In the right panel of Figure 6, we present the [CII]/TIR as a function of the TIR measured in this sample of DYNAMO galaxies. The magenta squares represent galaxies for which SEDs were used to derive the TIR, while the teal diamonds represent the galaxies for which the SFRs were

<sup>13</sup> https://github.com/aconley/mbb\_emcee

**Table 4**SOFIA [C II] and IR Measurements

Galaxy	22.2 μm (mJy)	89 μm (mJy)	155 μm (mJy)	216 μm (mJy)	$T_d$ (K)	TIR $(10^{10} L_{\odot})$	$\log_{10} L_{\text{[Cii]}} $ $(\text{erg s}^{-1})$
B08-3		•••	•••	•••	•••	•••	$41.82 \pm 0.46$
D10-4							$41.91 \pm 0.46$
D14-1	$12.3 \pm 3.5$	$148 \pm 19$	$423 \pm 47$	$209 \pm 25$	$25.94^{+5.10}_{-4.88}$	$3.48^{+0.69}_{-0.78}$	
D15-3	$8.1 \pm 2.8$	$282 \pm 33$	$393 \pm 44$	$685 \pm 73$	$29.56^{+3.06}_{-2.89}$	$4.26^{+0.52}_{-0.49}$	$41.74 \pm 0.46$
F08-2		$522 \pm 57$	$326 \pm 37$	$563 \pm 61$	$46.15^{+7.66}_{-6.72}$	$6.27^{+1.30}_{-1.34}$	$41.95 \pm 0.46$
F09-1	•••				•••	•••	$42.20 \pm 0.46$
F12-4	$15.3 \pm 3.9$	$224 \pm 27$	$279 \pm 32$	$594 \pm 64$	$23.43_{-7.05}^{+7.65}$	$4.11^{+0.74}_{-1.02}$	$42.21 \pm 0.46$

used instead. In both cases, we show error bars where the errors on the [CII] and TIR luminosities have been propagated into the ratio. The two approaches to estimating the TIR luminosities yield consistent results. To illustrate this, we join with black dashed lines the data points for which we have SEDs and SFRs. When we compare DYNAMO to existing measurements in different types of galaxies (Herrera-Camus et al. 2018a), we find that DYNAMO galaxies do not exhibit a [CII] deficit. Herrera-Camus et al. (2018a) showed that at a fixed IR luminosity, the [CII]/FIR ratio decreases as galaxies become more compact, and Lutz et al. (2016) showed that the line-to-FIR ratios form a much tighter relation with the FIR surface brightness than with luminosity. To investigate this, Herrera-Camus et al. (2018b) constructed two toy models with the PDR toolbox (Kaufman et al. 2006): one where OB stars are closely associated with molecular gas clouds, and another where OB stars and clouds are randomly distributed. They found that as galaxies become more compact, a combination of effects give rise to the [CII] deficit. These include a reduction in the photoelectric heating efficiency, an increase in the ionization parameter, and as the interstellar radiation field increases, the [CII] line saturates and becomes nearly independent of the far-UV flux. Although DYNAMO galaxies generally lie above the star-forming main sequence at  $z \sim 0.1$ , their star formation is distributed throughout their disks within numerous starforming clumps, rather than being confined to a compact region. Their low dust temperatures and lack of a [CII] deficit are consistent with this morphology.

# 4. Discussion

The  $\sim 1-2$  kpc scale ALMA observations allow us to investigate how the line ratios we measure are affected by the surface density of star formation. We expect that the CO(4-3)transition will be more highly excited in regions of higher  $\Sigma_{\rm SFR}$ , because these regions will have larger UV radiation fields and thus warmer dust temperatures (Narayanan & Krumholz 2014). To test this, we compare our resolved line ratio measurements to the  $\Sigma_{\rm SFR}$  measurements we take in the same beam-sized apertures. Figure 7 shows the CO(4-3)/CO(3-2) line ratio as a function of  $\Sigma_{SFR}$  for four galaxies for which all necessary observations are available, as indicated by the legend. For each galaxy, we plot the set of resolved beamsized measurements as previously described. Though the line ratio uncertainties are large, there is a moderate positive correlation between the line ratios and  $\Sigma_{\rm SFR}$  measurements, indicating that, in this sample of DYNAMO galaxies, higher  $\Sigma_{\rm SFR}$  regions are indeed correlated with higher line ratios. We perform a Spearman rank-order correlation and find a coefficient of  $\rho = 0.6$ . The correlation between resolved measurements within a single galaxy is stronger for DYNAMO D13-5 and G20-2 ( $\rho=0.8$ , 0.7, respectively), and weakest for DYNAMO G04-1 ( $\rho=0.4$ ), while for G14-1 it is  $\rho=0.6$ . In addition, we perform a linear fit to our observed line ratio— $\Sigma_{\rm SFR}$  relation using <code>scipy.curve\_fit</code>, which performs a nonlinear least squares analysis with errors on the y data as a parameter, and show the results with the black solid line. The black dashed line corresponds to the parameterization of CO line emission intensity as a function of  $\Sigma_{\rm SFR}$ , derived by Narayanan & Krumholz (2014; their Equation (19)):

$$\frac{I_{ij}}{I_{1-0}} = A \times [\log_{10}(\Sigma_{SFR}) - \chi]^{B} + C,$$
 (5)

where  $I_{ij}$  is the intensity of the CO(i-j) transition, A, B, and C are fit parameters, and  $\chi = -1.85$  (an offset introduced to produce only real values of  $I_{ij}/I_{1-0}$ ). Narayanan & Krumholz (2014) calculated the CO SLED of high-z star-forming galaxies from CO intensities that are modeled at  $\sim$ 70 pc resolution. For real observations with coarser beams, such as in our case, the resolved line ratio –  $\Sigma_{SFR}$  parameterization is not an appropriate comparison. Therefore, Narayanan & Krumholz (2014) determined the luminosity-weighted emitting area for each CO transition and scaled the resolved line intensities; then they refitted the line ratio- $\Sigma_{SFR}$  relation. Because our observations probe  $\sim$ 1-2 kpc scales, this is primarily what we compare to here. However, we show comparisons to the resolved parameterization for completeness We adopt values for A, B, and C for unresolved observations from their Table 3 for CO(3-2) and CO(4-3), and substitute in our measured values of  $\Sigma_{\rm SFR}$ . Finally, we take the ratio of the two equations and divide by  $J_u^2/J_l^2 = 4^2/3^2$  to convert from Jy to K and produce the dashed black line in Figure 7. We repeat the same procedure for the resolved galaxy observations parameterization from their Table 2 and plot this as the black dashed-dotted line in Figure 7.

Overall, both model parameterizations underpredict the steepness of the  $CO(4-3)/CO(3-2)-\Sigma_{SFR}$  relation that our observations suggest, and overpredict the line ratio across the entire range of  $\Sigma_{SFR}$  values that our observations probe. Similarly, Boogaard et al. (2020) found that the unresolved models also overpredict their CO(4-3)/CO(2-1) measurements (see their Figure 13), while providing a better match to their CO(5-4)/CO(2-1) values. Sharon et al. (2019), who presented  $\sim$ 2 kpc resolution CO(1-0) and CO(3-2) observations of a lensed galaxy at z=2.26, also found that the Narayanan & Krumholz (2014) models do not reproduce their observations; however, they do not attribute much meaning to

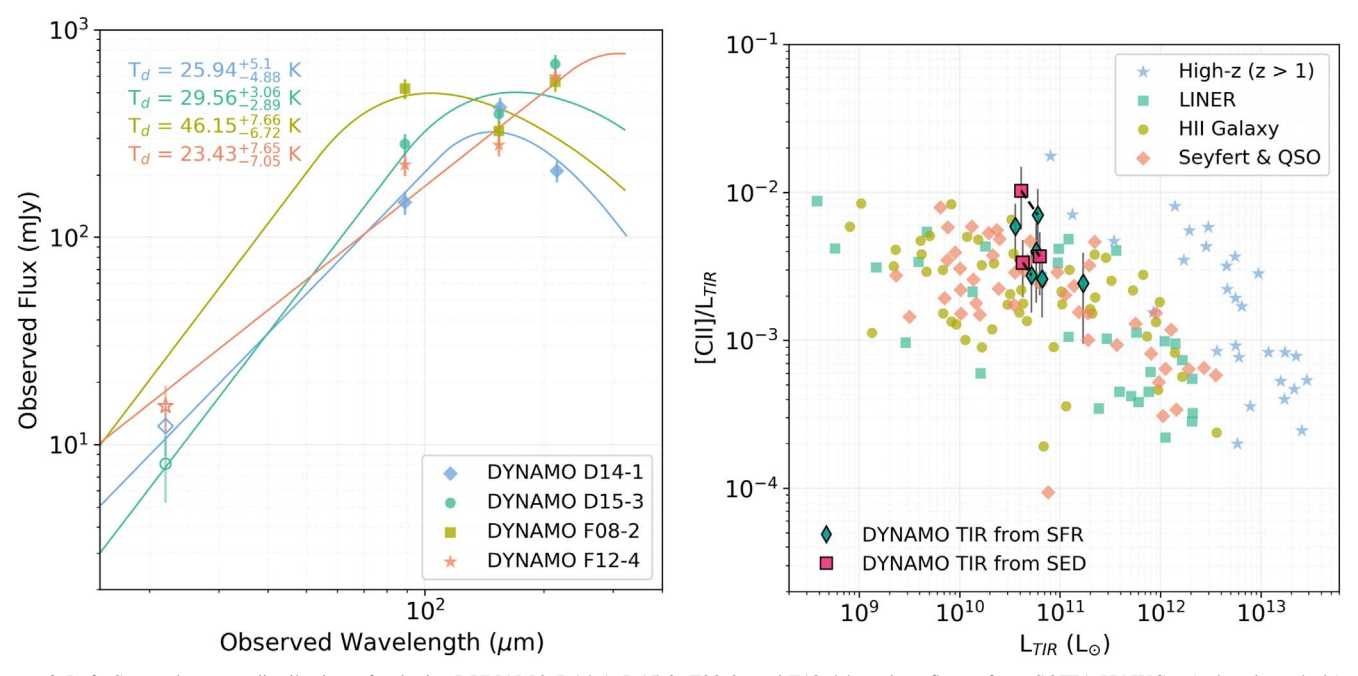


Figure 6. Left: Spectral energy distribution of galaxies DYNAMO D14-1, D15-3, F08-2, and F12-4 based on fluxes from SOFIA HAWC+ (colored symbols) and WISE observations (open colored symbols). The solid colored lines are the resulting SED fits using MBB\_EMCEE, with the corresponding dust temperatures appearing at the top left corner. For DYNAMO D14-1 and D15-3, the dust temperatures derived from the HAWC+ measurements are consistent with those derived by White et al. (2017) using Herschel PACS and SPIRE photometry. Right: The [CII]-to-TIR ratio as a function of the TIR. The colored symbols with black outlines correspond to DYNAMO measurements; the magenta symbols have TIR measurements derived from SED fitting, while the teal symbols have the TIR estimated from SFRs. For galaxies where we have both SED measurements and SFRs, we link the data points via a black dashed line. Grey error bars are the assumed 40% calibration uncertainty for the [CII] observations and TIR uncertainties propagated through the ratio. We compare our DYNAMO measurements to those of Herrera-Camus et al. (2018a) and find that DYNAMO galaxies do not show a deficit of [CII] emission, consistent with their cooler dust temperatures.

this difference due to the limited  $\Sigma_{\rm SFR}$  values probed by a single galaxy. In contrast, Valentino et al. (2020) found qualitative agreement between the unresolved Narayanan & Krumholz (2014) model and their CO(5-4)/CO(2-1) observations in z=1.1-1.7 IR-selected galaxies on and above the main sequence of star formation.

It is possible that because these models do not explicitly model gas-rich clumpy disks like DYNAMO and high-redshift star-forming galaxies, that their properties are not completely captured in the early-phase snapshots of the model disks and model mergers (Narayanan & Krumholz 2014). It is also possible that a model that characterizes global CO excitation properties for an average  $\Sigma_{\rm SFR}$  may not be well suited to investigate the internal variations within a single galaxy. To test this, we convolve our H $\alpha$  maps to the CO(1-0) beam sizes  $(\sim 5''-10'')$  of Fisher et al. (2019) and measure the global  $\Sigma_{\rm SFR}$ of each galaxy for which data are available. We then use Equation (5) and the unresolved parameters of Narayanan & Krumholz (2014) to predict  $R_{31}$  and  $R_{41}$ . We list these predictions in the last two columns of Table 3. We find that overall, the Narayanan & Krumholz (2014) models give better predictions of our global  $R_{31}$  and  $R_{41}$  measurements than our kiloparsec-scale  $R_{43}$  measurements, which may indicate that the unresolved models do not capture the kiloparsec-scale variation in CO excitation. Using hydrodynamical simulations, Bournaud et al. (2015) studied the CO SLEDs of high-redshift galaxies (as well as spirals and mergers) and investigated the contribution of giant clumps to the global CO SLED. They derive CO SLEDs for clumps and the interclump gas and show that there is a considerable difference in the CO excitation (see their Figures 3 and 4). This may indicate a need for models that specifically relate CO excitation, measured at various physical

scales, in gas-rich clumpy disks to observable quantities such as  $\Sigma_{\rm SFR}$ .

#### 5. Conclusions

In this work, we have combined  $\sim 1-2\,\mathrm{kpc}$  scale ALMA observations of CO(3-2) and CO(4-3) with HST observations of H $\alpha$ , to study the CO(4-3)/CO(3-2) line ratio and its dependence on  $\Sigma_{\mathrm{SFR}}$ . We have combined this with SOFIA HAWC+ and FIFI-LS observations of [CII], which provide additional measurements of the ISM gas physical conditions. We summarize our findings here:

- 1. DYNAMO galaxies have typical CO(4-3)/CO(3-2) line ratios of  $R_{43} = 0.54^{+0.16}_{-0.15}$ , which is most consistent with samples of star-forming  $\sim 1-2$  main-sequence galaxies (e.g., Daddi et al. 2015; Boogaard et al. 2020; Henríquez-Brocal et al. 2022).
- 2. Likewise, the global CO(3-2)/CO(1-0) and CO(4-3)/CO(1-0) measurements in DYNAMO are higher than global measurements of nearby star-forming galaxies (Leroy et al. 2022) and are more consistent with the measurements of  $z \sim 1-2$  star-forming galaxies (see, e.g., Daddi et al. 2015; Dessauges-Zavadsky et al. 2015; Birkin et al. 2021; Harrington et al. 2021).
- 3. The DYNAMO SEDs derived from SOFIA HAWC+ suggest cooler dust temperatures than those observed in local starburst galaxies and U/LIRGs. This suggests that, while DYNAMO galaxies are strongly star-forming, their star formation must be distributed rather than very compact. This is consistent with the picture we obtain from the CO(4-3)/CO(3-2) line ratio measurements and the clumpy morphology of these systems.

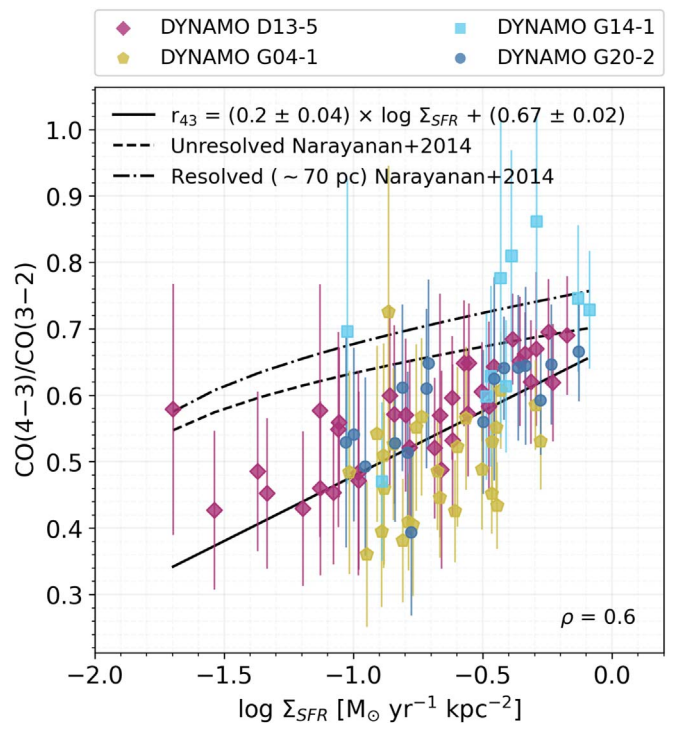


**Figure 7.** CO(4–3)/CO(3–2) line ratio as a function of the SFR surface density, measured in beam-sized regions across the disk of each galaxy, indicated by the color and symbol coding in the legend. We present these data for galaxies where observations of both CO transitions and H $\alpha$  exist. Despite the large uncertainties, there is an indication of an increasing line ratio with increasing SFR surface density trend. This is parameterized by Spearma's rank-order correlation coefficient of  $\rho=0.6$ , suggesting a moderate positive correlation between these two quantities. We present a linear fit to our measurements (black solid line) and for comparison, include the predicted trend using the unresolved relation between CO intensity and  $\Sigma_{\rm SFR}$  of Narayanan & Krumholz (2014; black dashed line), and their 70 pc resolved relations (black dashed–dotted line).

4. The DYNAMO CO(4-3)/CO(3-2) line ratios are positively correlated with the  $\Sigma_{SFR}$  measurements, with a Spearman rank-order correlation coefficient of  $\rho=0.6$ . Our best-fit relation between the CO(4-3)/CO(3-2) line ratio and  $\Sigma_{SFR}$  is  $R_{43}=(0.2\pm0.04)\times\log\Sigma_{SFR}+(0.67\pm0.02)$ . This relation suggests a steeper relation than predicted by the parameterization of Narayanan & Krumholz (2014), which also overpredicts the line ratio over the whole range of  $\Sigma_{SFR}$  values probed by observations. It is possible that this is consistent with the low dust temperatures of DYNAMO galaxies. However, Sharon et al. (2019), who also studied  $\sim$  kpc scale line ratios in a high-redshift lensed galaxy, also found a discrepancy between the models and observations. This may indicate that models that investigate CO

emission variations with internal galaxy properties for gas-rich clumpy disks are required.

We thank the anonymous referee for comments and suggestions that have greatly improved this work. This paper makes use of the following ALMA data: ADS/JAO.ALMA#2017.1.00239. S. and ADS/JAO/ALMA#2019.1.00447.S. ALMA is a partnership of ESO (representing its member states), NSF (USA) and NINS (Japan), together with NRC (Canada), MOST and ASIAA (Taiwan), and KASI (Republic of Korea), in cooperation with the Republic of Chile. The Joint ALMA Observatory is operated by ESO, AUI/NRAO and NAOJ. The National Radio Astronomy Observatory is a facility of the National Science Foundation operated under cooperative agreement by Associated Universities, Inc. Some of the data presented in this paper were obtained from the Mikulski Archive for Space Telescopes (MAST) at the Space Telescope Science Institute. The specific observations analyzed can be accessed via doi:10.17909/faa7-sw34. Based in part on observations made with the NASA/DLR Stratospheric Observatory for Infrared Astronomy (SOFIA). SOFIA is jointly operated by the Universities Space Research Association, Inc. (USRA), under NASA contract NNA17BF53C, and the Deutsches SOFIA Institut (DSI) under DLR contract 50 OK 0901 to the University of Stuttgart. Financial support for this work was provided by NASA through award #SOFIA-080238 issued by USRA. L.L. and A.D.B. acknowledges support from USRA SOFIA-080238 and NASA HSTGO15069002A, and NSF-AST2108140. R.C.L. acknowledges support from an NSF Astronomy and Astrophysics Postdoctoral Fellowship under award AST-2102625. D.O. is a recipient of an Australian Research Council Future Fellowship (FT190100083) funded by the Australian Government. R.H.-C. thanks the Max Planck Society for support under the Partner Group project "The Baryon Cycle in Galaxies" between the Max Planck for Extraterrestrial Physics and the Universidad de Concepción. R.H.-C. also acknowledges financial support from Millenium Nucleus NCN19058 (TITANs) and support by the ANID BASAL projects ACE210002 and FB210003. This research made use of Photutils, an Astropy package for detection and photometry of astronomical sources (Bradley et al. 2021).

Facilities: ALMA, HST(WFC), SOFIA(FIFI-LS, HAWC+). Software: aplpy (Robitaille 2019), astropy (Astropy Collaboration et al. 2013, 2018), CASA (McMullin et al. 2007), numpy (Harris et al. 2020), Photutils (Bradley et al. 2021), reproject (Robitaille 2018), spectral-cube (Ginsburg et al. 2019).

# Appendix A SOFIA Observations

We include here the integrated intensity maps of [CII] from FIFI-LS (Figure 8), and HAWC+ images (Figure 9) of the SOFIA DYNAMO sample.

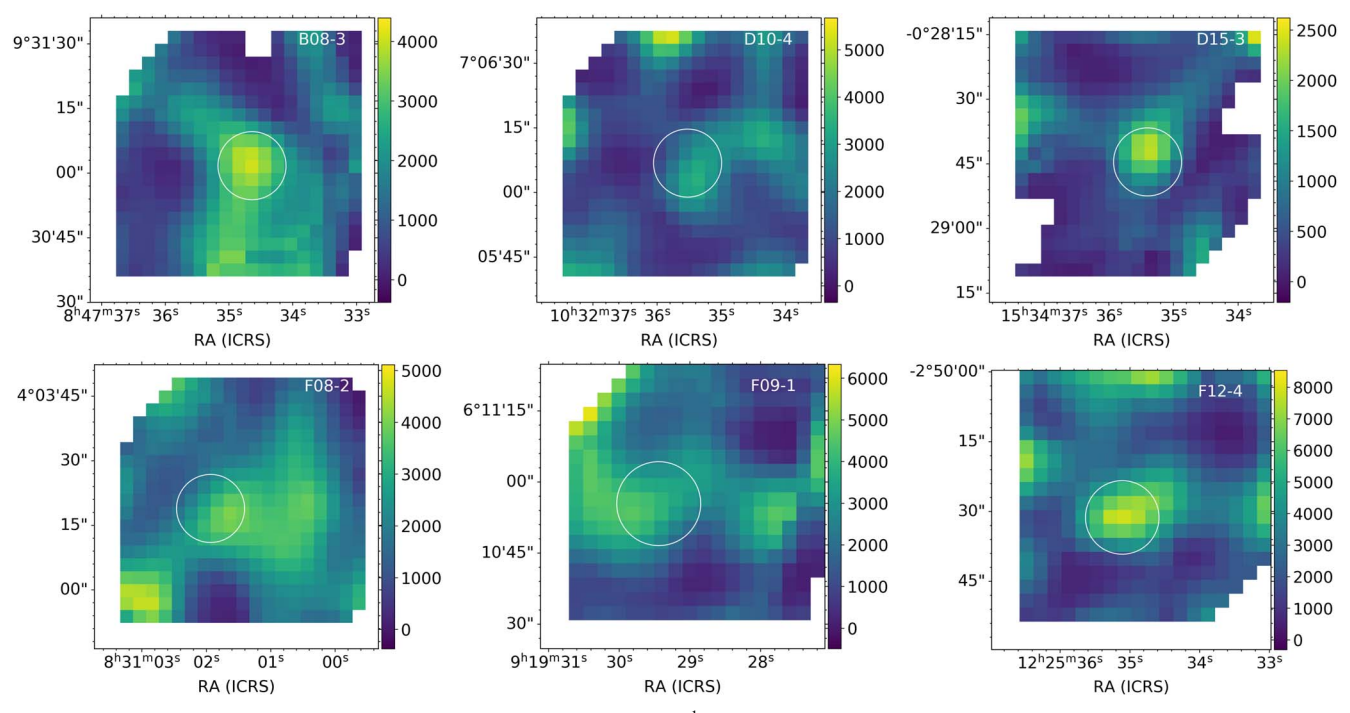


**Figure 8.** [CII] integrated intensity maps of DYNAMO galaxies in units of Jy km s $^{-1}$ . The white circle is centered on the DYNAMO galaxy, and its size corresponds to the angular resolution of the FIFI-LS instrument (15 $^{\prime\prime}_{-}$ 6). DYNAMO D15-3 (first row, rightmost panel) is the only galaxy that overlaps with the ALMA sample.

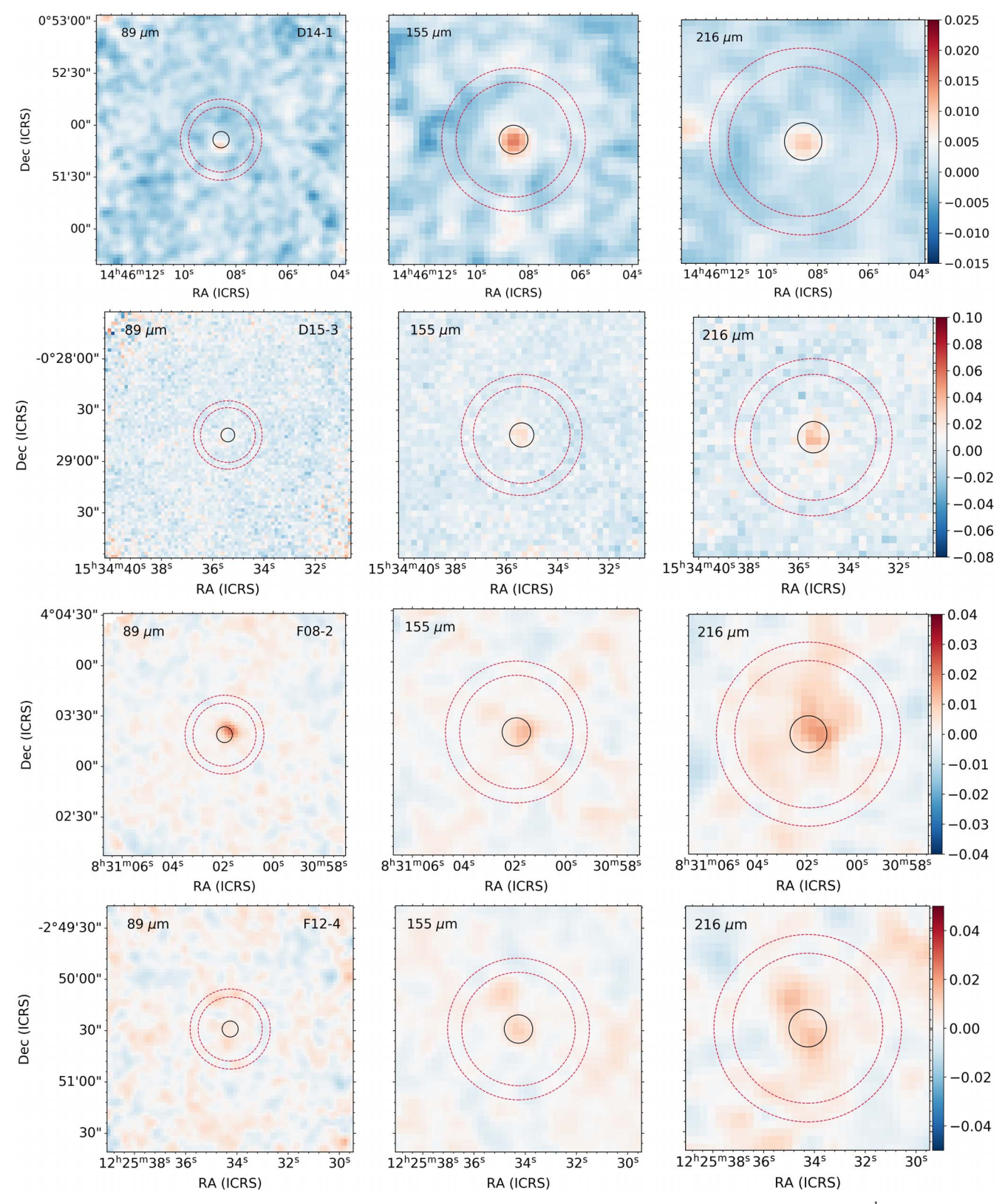


Figure 9. SOFIA HAWC+ observations of DYNAMO galaxies:  $89 \mu m$  (left),  $155 \mu m$  (middle), and  $216 \mu m$  (right) in units of Jy pixel<sup>-1</sup>. The black circles are centered on the position of the DYNAMO galaxy observed (indicated at the top right corner of the leftmost panels), and their size corresponds to the angular resolution of each band (wavelength is indicated at the top left corner of each panel). The crimson dashed circles define the background annulus. DYNAMO D15-3 (second row) is the only galaxy that overlaps with the ALMA sample.

# Appendix B Line Ratio Literature Compilation

Daddi et al. (2015) used IRAM PdBI observations of CO(2-1), CO(3-2), and CO(5-4), and Very Large Array observation of CO(1-0) in three main-sequence star-forming disk galaxies at  $z \sim 1.5$  to study their CO excitations. We use their average  $R_{31}$  and interpolate their models from their Figure 10 to extract  $R_{41}$ , then take the ratio  $R_{41}/R_{31}$  to obtain  $R_{43} = 0.74 \pm 0.26$ , which we include in Figure 4 as a black circle.

Kamenetzky et al. (2016) found a linear relation between  $L_{\rm FIR}$  and  $L'_{\rm CO}$  for low- to mid-J CO lines and a slightly sublinear relation for high-J CO lines. We adopt the slope and intercepts of the relations for CO(4–3) and CO(3–2) from their Tables 6 and 7 (for U/LIRGs and non-U/LIRGs ( $L_{\rm FIR} \le 6 \times 10^{10} \, L_{\odot}$ ), respectively), and assume an FIR luminosity of  $10^{11}$  for the U/LIRG case and  $10^{10}$  for the non-U/LIRG case to derive the  $L_{\rm FIR} - L'_{\rm CO}$  relations. Taking the ratio of these we find  $R_{43} = 0.51 \pm 0.10$  and  $0.25 \pm 0.05$  for U/LIRGs and non-U/LIRGs, respectively, assuming a 20% uncertainty. We plot these as black stars in Figure 4.

Rosenberg et al. (2015) studied the CO SLEDs of 29 U/LIRGs from CO(1–0) through CO(13–12). They classify their objects into three classes based on their excitation level. Where available, we compiled CO(4–3) and CO(3–2) fluxes from their Tables 2 and 3, and divided the resulting ratios by  $(J_u^3/J_l^3)$  to convert from units of W m<sup>-2</sup> to K. Finally, we separated the galaxies according to their classification, and plot the median line ratio for each class as black diamonds in Figure 4. The error bars represent the standard deviation of line ratios in each class to illustrate the spread. We note that most of the Rosenberg et al. (2015) sample is contained within the Kamenetzky et al. (2016) sample.

Papadopoulos et al. (2012) studied the CO SLEDs of 70 U/LIRGs; we averaged the  $R_{43}$  values from their Table 7 (eight galaxies in total) and calculated the standard error on the mean. This results in  $R_{43} = 0.96 \pm 0.12$ ; we plot this as a black pentagon in Figure 4. We note that 11/70 galaxies from the Papadopoulos et al. (2012) sample overlap with the sample of Rosenberg et al. (2015).

Finally, Henríquez-Brocal et al. (2022) combined NOEMA observations of [CI](1–0), [CI](2–1), and CO(7–6) with ancillary CO(1–0) and CO(3–2) observations to model the CO SLED of Q1700-MD94, a massive main-sequence galaxy at  $z \sim 2$ , with a one- and two-temperature component model using RADEX (van der Tak et al. 2007). We interpolate the model curves in their Figure 3 to extract  $R_{43} = 0.92 \pm 0.18$  and  $0.77 \pm 0.15$  for the one- and two-component models, respectively (taking a 20% uncertainty). We do not plot these values in Figure 4, but include them in Table 2.

#### **ORCID iDs**

Laura Lenkić https://orcid.org/0000-0003-4023-8657
Alberto D. Bolatto https://orcid.org/0000-0002-5480-5686
Deanne B. Fisher https://orcid.org/0000-0003-0645-5260
Roberto Abraham https://orcid.org/0000-0002-4542-921X
Karl Glazebrook https://orcid.org/0000-0002-3254-9044
Rodrigo Herrera-Camus https://orcid.org/0000-0002-2775-0595

Rebecca C. Levy https://orcid.org/0000-0003-2508-2586 Danail Obreschkow https://orcid.org/0000-0002-1527-0762

#### References

```
Adelman-McCarthy, J. K., Agüeros, M. A., Allam, S. S., et al. 2006, ApJS,
   162, 38
Ambachew, L., Fisher, D. B., Glazebrook, K., et al. 2022, MNRAS, 512, 3079
Aravena, M., Hodge, J. A., Wagg, J., et al. 2014, MNRAS, 442, 558
Astropy Collaboration, Price-Whelan, A. M., Sipőcz, B. M., et al. 2018, AJ,
Astropy Collaboration, Robitaille, T. P., Tollerud, E. J., et al. 2013, A&A,
   558, A33
Barvainis, R., Maloney, P., Antonucci, R., & Alloin, D. 1997, ApJ, 484, 695
Bassett, R., Glazebrook, K., Fisher, D. B., et al. 2014, MNRAS, 442, 3206
Bassett, R., Glazebrook, K., Fisher, D. B., et al. 2017, MNRAS, 467, 239
Bennett, C. L., Larson, D., Weiland, J. L., & Hinshaw, G. 2014, ApJ, 794, 135
Birkin, J. E., Weiss, A., Wardlow, J. L., et al. 2021, MNRAS, 501, 3926
Bolatto, A. D., Warren, S. R., Leroy, A. K., et al. 2015, ApJ, 809, 175
Boogaard, L. A., Werf, P. v. d., Weiss, A., et al. 2020, ApJ, 902, 109
Bothwell, M. S., Smail, I., Chapman, S. C., et al. 2013, MNRAS, 429, 3047
Bournaud, F., Daddi, E., Weiß, A., et al. 2015, A&A, 575, A56
Bradley, L., Sipöcz, B., Robitaille, T., et al. 2021, astropy/photutils: 1.2.0,
   Zenodo, doi:10.5281/zenodo.5525286
Brauher, J. R., Dale, D. A., & Helou, G. 2008, ApJS, 178, 280
Brisbin, D., Aravena, M., Daddi, E., et al. 2019, A&A, 628, A104
Calzetti, D. 2013, in Secular Evolution of Galaxies, ed. J. Falcón-Barroso &
   J. H. Knapen (Cambridge: Cambridge Univ. Press), 419
Cardelli, J. A., Clayton, G. C., & Mathis, J. S. 1989, ApJ, 345, 245
Carilli, C. L., & Walter, F. 2013, ARA&A, 51, 105
Cluver, M. E., Jarrett, T. H., Dale, D. A., et al. 2017, ApJ, 850, 68
Colditz, S., Beckmann, S., Bryant, A., et al. 2018, JAI, 7, 1840004
Daddi, E., Bournaud, F., Walter, F., et al. 2010, ApJ, 713, 686
Daddi, E., Dannerbauer, H., Liu, D., et al. 2015, A&A, 577, A46
Decarli, R., Walter, F., Aravena, M., et al. 2016, ApJ, 833, 70
Decarli, R., Walter, F., Carilli, C., et al. 2014, ApJ, 782, 78
Decarli, R., Walter, F., Gónzalez-López, J., et al. 2019, ApJ, 882, 138
den Brok, J. S., Chatzigiannakis, D., Bigiel, F., et al. 2021, MNRAS, 504, 3221
Dessauges-Zavadsky, M., Zamojski, M., Rujopakarn, W., et al. 2017, A&A,
   605, A81
Dessauges-Zavadsky, M., Zamojski, M., Schaerer, D., et al. 2015, A&A,
  577, A50
Dowell, C. D., Conley, A., Glenn, J., et al. 2014, ApJ, 780, 75
Fischer, C., Beckmann, S., Bryant, A., et al. 2018, JAI, 7, 1840003
Fisher, D. B., Bolatto, A. D., White, H., et al. 2019, ApJ, 870, 46
Fisher, D. B., Glazebrook, K., Abraham, R. G., et al. 2017b, ApJL, 839, L5
Fisher, D. B., Glazebrook, K., Bolatto, A., et al. 2014, ApJL, 790, L30
Fisher, D. B., Glazebrook, K., Damjanov, I., et al. 2017a, MNRAS, 464, 491
Fixsen, D. J., Bennett, C. L., & Mather, J. C. 1999, ApJ, 526, 207
Förster Schreiber, N. M., Genzel, R., Lehnert, M. D., et al. 2006, ApJ,
Förster Schreiber, N. M., Shapley, A. E., Genzel, R., et al. 2011, ApJ, 739, 45
Freundlich, J., Combes, F., Tacconi, L. J., et al. 2019, A&A, 622, A105
Genzel, R., Tacconi, L. J., Gracia-Carpio, J., et al. 2010, MNRAS, 407, 2091
Genzel, R., Tacconi, L. J., Lutz, D., et al. 2015, ApJ, 800, 20
Ginsburg, A., Koch, E., Robitaille, T., et al. 2019, radio-astro-tools/spectral-
   cube: Release v0.4.5, Zenodo, doi:10.5281/zenodo.3558614
Girard, M., Fisher, D. B., Bolatto, A. D., et al. 2021, ApJ, 909, 12
Green, A. W., Glazebrook, K., McGregor, P. J., et al. 2014, MNRAS,
   437, 1070
Greve, T. R., Leonidaki, I., Xilouris, E. M., et al. 2014, ApJ, 794, 142
Guo, Y., Ferguson, H. C., Bell, E. F., et al. 2015, ApJ, 800, 39
Guo, Y., Rafelski, M., Bell, E. F., et al. 2018, ApJ, 853, 108
Hao, C.-N., Kennicutt, R. C., Johnson, B. D., et al. 2011, ApJ, 741, 124
Harper, D. A., Runyan, M. C., Dowell, C. D., et al. 2018, JAI, 7, 1840008
Harrington, K. C., Weiss, A., Yun, M. S., et al. 2021, ApJ, 908, 95
Harris, C. R., Millman, K. J., van der Walt, S. J., et al. 2020, Natur, 585, 357
Henríquez-Brocal, K., Herrera-Camus, R., Tacconi, L., et al. 2022, A&A,
   657, L15
Herrera-Camus, R., Sturm, E., Graciá-Carpio, J., et al. 2018a, ApJ, 861, 94
Herrera-Camus, R., Sturm, E., Graciá-Carpio, J., et al. 2018b, ApJ, 861, 95
Kamenetzky, J., Glenn, J., Rangwala, N., et al. 2012, ApJ, 753, 70
Kamenetzky, J., Rangwala, N., Glenn, J., Maloney, P. R., & Conley, A. 2016,
Kaufman, M. J., Wolfire, M., & Hollenbach, D. J. 2006, ApJ, 644, 283
Klitsch, A., Christensen, L., Valentino, F., et al. 2022, MNRAS, 514, 2346
Koda, J., Scoville, N., Hasegawa, T., et al. 2012, ApJ, 761, 41
Kroupa, P. 2001, MNRAS, 322, 231
Lagos, C. d., Bayet, E., Baugh, C. M., et al. 2012, MNRAS, 426, 2142
```

Zenodo, doi:10.5281/zenodo.1162674

```
Lenkić, L., Bolatto, A. D., Fisher, D. B., et al. 2021, MNRAS, 506, 3916
Lenkić, L., Bolatto, A. D., Förster Schreiber, N. M., et al. 2020, AJ, 159, 190
Leroy, A. K., Rosolowsky, E., Usero, A., et al. 2022, ApJ, 927, 149
Leroy, A. K., Walter, F., Bigiel, F., et al. 2009, AJ, 137, 4670
Leroy, A. K., Walter, F., Sandstrom, K., et al. 2013, AJ, 146, 19
Levy, R. C., Bolatto, A. D., Teuben, P., et al. 2018, ApJ, 860, 92
Lord, S. D. 1992, A New Software Tool For Computing Earth's Atmospheric
   Transmission Of Near- And Far-infrared Radiation, NASA Technical
   Memorandum 103957, NASA
Lutz, D., Berta, S., Contursi, A., et al. 2016, A&A, 591, A136
Malhotra, S., Kaufman, M. J., Hollenbach, D., et al. 2001, ApJ, 561, 766
McMullin, J. P., Waters, B., Schiebel, D., Young, W., & Golap, K. 2007, in
   ASP Conf. Ser. 376, Astronomical Data Analysis Software and Systems
   XVI, ed. R. A. Shaw, F. Hill, & D. J. Bell (San Francisco, CA: ASP), 127
Narayanan, D., & Krumholz, M. R. 2014, MNRAS, 442, 1411
Obreschkow, D., Glazebrook, K., Bassett, R., et al. 2015, ApJ, 815, 97
Obreschkow, D., Heywood, I., Klöckner, H.-R., & Rawlings, S. 2009, ApJ,
   702, 1321
Oliva-Altamirano, P., Fisher, D. B., Glazebrook, K., et al. 2018, MNRAS,
   474, 522
Papadopoulos, P. P., van der Werf, P. P., Xilouris, E. M., et al. 2012, MNRAS,
   426, 2601
Popping, G., Pérez-Beaupuits, J. P., Spaans, M., Trager, S. C., &
   Somerville, R. S. 2014, MNRAS, 444, 1301
Riechers, D. A., Boogaard, L. A., Decarli, R., et al. 2020, ApJL, 896, L21
Riechers, D. A., Bradford, C. M., Clements, D. L., et al. 2013, Natur, 496, 329
Riechers, D. A., Pavesi, R., Sharon, C. E., et al. 2019, ApJ, 872, 7
Robitaille, T. 2018, reproject: astronomical image reprojection in Python, v0.4,
```

```
Robitaille, T. 2019, APLpy v2.0: The Astronomical Plotting Library in Python,
  Zenodo, doi:10.5281/zenodo.2567476
Rosenberg, M. J. F., van der Werf, P. P., Aalto, S., et al. 2015, ApJ, 801, 72
Sakamoto, S., Hasegawa, T., Handa, T., Hayashi, M., & Oka, T. 1997, ApJ,
  486, 276
Sawada, T., Hasegawa, T., Handa, T., et al. 2001, ApJS, 136, 189
Sharon, C. E., Tagore, A. S., Baker, A. J., et al. 2019, ApJ, 879, 52
Smith, J. D. T., Croxall, K., Draine, B., et al. 2017, ApJ, 834, 5
Solomon, P. M., Downes, D., Radford, S. J. E., & Barrett, J. W. 1997, ApJ,
  478, 144
Soto, E., Mello, D. F. d., Rafelski, M., et al. 2017, ApJ, 837, 6
Spilker, J. S., Marrone, D. P., Aguirre, J. E., et al. 2014, ApJ, 785, 149
Tacconi, L. J., Genzel, R., Neri, R., et al. 2010, Natur, 463, 781
Tacconi, L. J., Genzel, R., & Sternberg, A. 2020, ARA&A, 58, 157
Tacconi, L. J., Neri, R., Genzel, R., et al. 2013, ApJ, 768, 74
Tremonti, C. A., Heckman, T. M., Kauffmann, G., et al. 2004, ApJ, 613, 898
Übler, H., Genzel, R., Wisnioski, E., et al. 2019, ApJ, 880, 48
Vacca, W., Clarke, M., Perera, D., Fadda, D., & Holt, J. 2020, in ASP Conf.
   Ser. 527, Astronomical Data Analysis Software and Systems XXIX, ed.
   R. Pizzo et al. (San Francisco, CA: ASP), 547
Valentino, F., Daddi, E., Puglisi, A., et al. 2020, A&A, 641, A155
van der Tak, F. F. S., Black, J. H., Schoier, F. L., Jansen, D. J., &
  van Dishoeck, E. F. 2007, A&A, 468, 627
van der Werf, P. P., Isaak, K. G., Meijerink, R., et al. 2010, A&A, 518, L42
Walter, F., Decarli, R., Aravena, M., et al. 2016, ApJ, 833, 67
Walter, F., Decarli, R., Sargent, M., et al. 2014, ApJ, 782, 79
White, H. A., Fisher, D. B., Abraham, R. G., Glazebrook, K., &
  Obreschkow, D. 2022, ApJ, 926, 32
White, H. A., Fisher, D. B., Murray, N., et al. 2017, ApJ, 846, 35
```